Coupled hydro-mechanical modelling of soil-vegetation-atmosphere interaction in natural clay slopes

Pedone Giuseppe, Tsiampousi Aikaterini, Cotecchia Federica, Zdravkovic Lidija

Abstract

Soil-vegetation-atmosphere interaction is long known to induce significant pore pressure variations at shallow depths and associated superficial slope movements. Recent findings suggest that the effect of this interaction may also extend to large depths in natural clay slopes. Multiple examples of weather-induced deep landslide mechanisms can be found in the Southern Apennines (Italy), where slopes are often formed of fissured clays. The relationship between the activity of these landslides and the hydro-mechanical processes due to soil-vegetation-atmosphere interaction was investigated herein by means of a two-dimensional coupled hydro-mechanical finite element analysis. A constitutive model capable of simulating the behaviour of highly overconsolidated clays, in both saturated and unsaturated states, was adopted in the analysis, in conjunction with a boundary condition capable of reproducing the combined effects of rainfall infiltration, evapo-transpiration and run-off. The results of the analysis corroborate the connection between weather conditions, pore pressure variations and slope movements in natural clay slopes. The importance of reproducing adequately the geological history of a natural slope in order to define its current state is also demonstrated.

Key words: numerical modelling; finite element analysis; soil-vegetation-atmosphere interaction; natural slopes; landslides; fissured clays.

Words: 6660

Tables: 3

Figures: 15

Word equivalents (counting 250 words for each Table and Figure): 11160

© The Author(s) or their Institution(s)

Draft

Introduction

Soil-atmosphere interaction has been extensively investigated in the laboratory and in the field (e.g. Blight 1997; Toll et al. 2011; Smethurst et al. 2012; Pirone et al. 2015; Askarinejad et al. 2018; Stirling et al. 2020), as well as through physical and numerical modelling (e.g. Kovacevic et al. 2001; Gens 2010; Take and Bolton 2011; Elia et al. 2017). Soil-atmosphere interaction depends on the thermo-hydro-mechanical properties of the soil (e.g. retention behaviour, hydraulic conductivity and constitutive law), but also on climatic factors such as atmospheric pressure, relative humidity, temperature, rainfall, net solar radiation and wind. Vegetation interferes with soil-atmosphere interaction due to processes such as interception and transpiration, configuring what is known as 'soil-vegetation-atmosphere interaction' (e.g. Nyambayo and Potts 2010; Tsiampousi et al. 2017*a*; Switala and Wu 2018; Capobianco et al. 2020; Rouania et al. 2020; Woodman et al. 2020).

Soil-vegetation-atmosphere interaction can induce significant pore pressure variations in the soil, which may, in turn, cause slope instabilities, as documented by several authors (e.g. Leroueil 2001; Cascini et al. 2010; Pirone et al. 2012; Sitarenios et al. 2019). However, the case studies reported in the literature seldom concern deep landslide activity in clay slopes, for which soil-vegetation-atmosphere interaction effects have been for long considered negligible, especially at depths larger than 10 m (e.g. Kenney and Lau 1984; Vaughan 1994). Nonetheless, recent findings indicate that, in clay slopes, climate can induce pore pressure variations and associated slope movements also at intermediate (10-30 m) to large (30-100 m) depths (e.g. Tommasi et al. 2013; Vassallo et al. 2015; Cotecchia et al. 2014; 2015; 2016; Lollino et al. 2016; Pedone et al. 2018).

The Southern Apennines (Italy), where several slopes have been monitored continuously in the last two decades (e.g. Fontana Monte slope, Lollino et al 2016; Pianello slope, Palmisano et al 2018; Pisciolo slope, Cotecchia et al 2014), is of particular interest when studying the effects of soil-vegetation-atmosphere interaction on deep landslide movements. The weather conditions affecting this area are representative of the whole Mediterranean climatic region (Peel et al. 2007), where dry

© The Author(s) or their Institution(s)

and warm seasons alternate with rainy and cold ones, causing piezometric head increases from early autumn to early spring, and subsequent piezometric head reductions until the end of summer (e.g. Cotecchia et al. 2014; 2015; 2016). As example, Figure 1 shows data recorded within the Pisciolo and the Pianello clay slopes (modified from Cotecchia et al. 2014), where pore pressure fluctuations as high as 50 kPa were recorded up to 60 m depth. The consequent seasonal variation of the soil shear strength at depth can be inferred from the deep movements recorded on site, the latter also reported in Figure 1.

The displacement rates shown in Figure 1a were logged at Pisciolo at ground level and at around 18 m depth through a GPS antenna (G2) and an inclinometer (I12), respectively. The locations of G2 and I12 are indicated in Figure 2, where the map and the cross-section A-A′ of the slope are shown. The monitoring data collected at Pisciolo describe the activity of a deep multiple roto-translational landslide mechanism (Figure 2), classified as slow to extremely slow according to Hungr et al. (2014). Displacement rates like those shown in Figure 1a are recurrently recorded in multiple clay slopes in the Southern Apennines (e.g. Figure 1b for the Pianello case study), causing significant damage to infrastructures and structures. At Pisciolo, for instance, a road and a 2 m diameter water main (indicated in Figure 2) were repeatedly damaged in the last two decades (as reported by Cotecchia et al 2014), urging the use of advanced numerical modelling to inform current understanding of the complex mechanisms taking place and to underpin the development of mitigation measures.

Figure 1 also shows the 180 days cumulative rainfalls measured in the proximity of the Pisciolo and the Pianello slopes. The pattern of rainfall data is similar to the patterns observed both for piezometric levels and displacement rates. According to Cotecchia et al. (2014), this suggests that soil-vegetation-atmosphere interaction represents one of the main factors dominating the landslide activity in the slopes of the Southern Apennines formed of clayey turbidites. This interpretation was supported by results of finite element hydraulic analyses undertaken by Cotecchia et al. (2014) to investigate the soil-vegetation-atmosphere interaction processes occurring at Pisciolo. These results suggest that

© The Author(s) or their Institution(s)

significant pore pressure changes can be mobilised also at large depths in slopes formed of fissured clays, especially when they interbed highly permeable rock or coarse inclusions.

Although the transient seepage processes induced in slopes by atmospheric variations can be explored by means of hydraulic analyses, weather-induced slope movements can only be investigated in coupled hydro-mechanical analyses, which are rarely reported in the literature for natural clay slopes (e.g. Davies et al. 2014). The present work aims to provide insight into the hydro-mechanical processes active in natural clay slopes due to soil-vegetation-atmosphere interaction through an advanced coupled modelling application. To this aim, the paper presents a two-dimensional plane strain hydro-mechanically coupled finite element analysis of a typical slope located in the Southern Apennines. The main features of the case study inspiring the modelling, i.e. the Pisciolo slope, are first summarised. Subsequently, the key elements of the analysis are described, and its results discussed.

Draft

Geological and geo-morphological setting of the Pisciolo slope

The model for a generic clay slope, representative of the Southern Apennines, was developed to investigate the complex processes resulting from soil-vegetation-atmosphere interaction. The Pisciolo case study (latitude 41°00’35’’ N, longitude 15°34’15’’ E), extensively discussed by Cotecchia et al. (2014), and in particular section A-A′ shown in Figure 2, served as a reference in the modelling, and were used to derive representative geological and geo-morphological conditions.

The slopes primarily affected by soil-vegetation-atmosphere interaction in mountainous chains like the Southern Apennines typically lie in a river valley. As such, the materials forming the slope are expected to have undergone major lateral compression and shearing due to tectonic processes occurring during orogenesis. Furthermore, after orogenesis, the slope morphology often evolved due to river erosion at the toe. These elements of the slope’s history were carefully considered when defining the initial hydro-mechanical conditions of the slope model.

© The Author(s) or their Institution(s)

Several factors usually contribute to landslide activation in the Southern Apennines, not only the soil-vegetation-atmosphere interaction. This is also the case at Pisciolo, where the failure mechanism formed by the landslide bodies C9, C and A, shown in Figure 2, was initially triggered by three-dimensional geo-morphological and hydro-geological changes. According to Cotecchia et al. (2014), body C9 represented the first-time failure, whose retrogression caused the formation of body C. A further retrogression is currently taking place, promoting the development of body A, as indicated by movements recorded up to 60 m of depth down inclinometer I5 (indicated in Figure 2). The numerical analysis presented in the following investigates whether the first activation of progressive failure in clay slopes similar to Pisciolo may result from all the processes that led to the formation and the evolution of these slopes, including their geological history and their interaction with the atmosphere.

Several slopes in the Southern Apennines are formed of clayey turbidites, typically consisting of structurally complex clays interbedding coarse or fractured rock inclusions. However, since slope failures usually develop through the clay component of these turbiditic formations, the generic slope herein considered was assumed to be formed of clay materials only. In particular, the clays forming the Paola Doce turbidite, involved in the Pisciolo landslide, were taken as a reference.

Draft

Physical, mechanical and hydraulic properties of the Paola Doce clay

The Paola Doce clay at Pisciolo is very heterogeneous (clay fraction 37-62%, silt fraction 30-40%), highly plastic (plasticity index 33-45%) and intensely fissured (Cotecchia et al. 2014). Following Vitone and Cotecchia (2011) and Vitone et al. (2013a; 2013b), given the very high fissuring intensity of the material (i.e. fissure spacing of a few millimetres), its bulk behaviour can be characterised following traditional continuum mechanics approaches.

Figure 3 shows the void ratio, e, measured on undisturbed Paola Doce clay samples extracted, from different depths, in the proximity of section A-A′ in Figure 2. These samples were found to be highly

© The Author(s) or their Institution(s)

overconsolidated when subjected to oedometric compression, as seen, for example, in Figure 4a, showing the oedometer test data for a specimen taken at around 10 m depth. The average overconsolidation ratio, OCR, defined as ratio between vertical effective stress at yield and current vertical effective stress, σ'_{vy}/σ'_{v}, ranged between 4 and 8.

Several fully saturated samples were subjected to triaxial compression, exhibiting a dilative and mildly strain softening response after consolidation to mean effective stresses representative of in situ conditions. Assuming an effective cohesion intercept at peak, c'_{peak}, equal to 0 kPa, the average effective angles of shear resistance at peak, φ'_{peak}, range between 16.1° and 25.3° for initial mean effective stresses, p', lower than 300 kPa. These peak drained shear strengths are variable, reflecting the heterogeneity shown by the Paola Doce clay, and they are also low, therefore representing an internal factor predisposing the Pisciolo slope to failure (as discussed by Cotecchia et al. 2015). As an example, the results of an undrained triaxial test conducted on a specimen isotropically consolidated up to p' = 295 kPa are reported in Figures 4b and 4c.

The average saturated hydraulic conductivity, k_{sat}, measured during oedometer consolidation testing of undisturbed Paola Doce clay samples is around 10^{-10} m/s (as shown in Figure 5). However, field permeabilities larger than 10^{-9} m/s were measured through constant head hydraulic conductivity tests (Figure 5) carried out by Pedone (2014) in Casagrande piezometers installed within borehole P1 in Figure 2.

Figure 6a shows water retention data collected through unconfined drying tests performed by Pedone (2014) on undisturbed samples taken between 0.5 m and 1.5 m depth in the area indicated as S in Figure 2. The suctions were measured using both the filter paper technique (e.g. Marinho and Oliveira 2006) and high capacity tensiometers (e.g. Ridley and Burland 1993). The samples exhibited an initial degree of saturation, S_r, lower than 95% even at suctions lower than 50 kPa, due to air entering the fissures. During drying, however, S_r started reducing significantly only at suctions larger than 1 MPa,

© The Author(s) or their Institution(s)

when also major volumetric deformations were measured. This suction threshold is defined as 'gross' air-entry value by Cafaro and Cotecchia (2015).

Hydro-mechanical numerical modelling of the Paola Doce clay

The hydro-mechanical numerical model described in the paper was developed using the finite element (FE) code ICFEP (Potts and Zdravkovic 1999). ICFEP allows for a fully coupled hydro-mechanical modelling of the consolidation processes taking place in unsaturated soils by adopting a formulation based on the theory proposed by Biot (1941). The governing equations implemented in ICFEP are solved by means of a modified Newton-Raphson solution technique, which incorporates an error controlled sub-stepping stress-point algorithm (Potts and Ganendra 1994). These equations, described in detail by Potts and Zdravkovic (1999) with reference to fully saturated conditions, were extended to model the behaviour of unsaturated soils, as described by Smith (2003), Tsiampousi et al. (2017*b*) and Zdravkovic et al. (2018).

Draft

The hydro-mechanical behaviour of the Paola Doce clay was simulated with the constitutive model proposed by Tsiampousi et al. (2013*a*), which is an extended version of the model developed by Georgiadis et al. (2005) on the basis of the Barcelona Basic Modelling framework (Alonso et al. 1990). Principally, the former model introduces the Hvorslev surface on the dry side of critical state as an additional model flexibility for describing the yielding of highly overconsolidated clays. The selection of the model for this study was also driven by the need to simulate the unsaturated state of the clay, should the magnitudes of suction in the analysis of the slope develop beyond the air-entry value.

The model adopts the effective stress principle when the matrix suction, s, is smaller than the air-entry value, s_{air}. In this case, the model performs in the generalised stress space J-p'-θ, where θ is the Lode's angle, p' is the mean effective stress, and J is the generalised deviatoric stress invariant, the latter defined as

© The Author(s) or their Institution(s)

(1) $$J = \sqrt{\frac{1}{6}\left[(\sigma'_x - \sigma'_y)^2 + (\sigma'_y - \sigma'_z)^2 + (\sigma'_z - \sigma'_x)^2\right] + \tau_{xy}^2 + \tau_{xz}^2 + \tau_{yz}^2}$$

For suctions beyond the air-entry value, s_{air}, the model adopts two independent stress variables

(a) the equivalent suction, s_{eq}

(2) $$s_{eq} = s - s_{air}$$

(b) the equivalent net stress, σ_{eq}

(3) $$\sigma_{eq} = \sigma_{net} + s_{air}$$

where the net stress, σ_{net}, corresponds to the excess of the total stress, σ_{tot}, over the pore air pressure, u_a. When $s > s_{air}$, the model performs in the generalised stress space J-p-θ-s_{eq}, with all the invariants calculated in terms of equivalent net stresses. The values of the constitutive model parameters used in the slope analysis are summarised in Table 1 and their calibration is described in the following.

The yield and plastic potential functions adopted on the wet side of critical state (Figure 7a) correspond to those proposed originally by Georgiadis et al. (2005) (extending the expressions of Lagioia et al. 1996). They are defined by the parameters $\alpha_{f,g}$, $\mu_{f,g}$ and $M_{f,g}$, where the subscripts f and g refer to the yield function and the plastic potential function, respectively. On the dry side, the non-linear Hvorslev surface introduced by Tsiampousi et al. (2013*a*) was employed (Figure 7a), whose shape is defined by the parameters α_{HV}, n_{HV}, β_{HV} and m_{HV}. The model adopts the Matsuoka and Nakai (1974) failure criterion in the deviatoric plane, which simulates more accurately the soil strength under non-triaxial compression loading.

The data from undrained triaxial tests performed on fully saturated samples were used to calibrate the yield and plastic potential functions. Figures 4b and 4c illustrate a comparison between experimental data and numerical predictions for a representative undrained triaxial test conducted on a specimen with an overconsolidation ratio, R = 4 (defined as ratio between mean effective stress at yield and

© The Author(s) or their Institution(s)

current mean effective stress, p'_y/p'). With reference to the compression behaviour, κ, λ and v_1 were estimated based on oedometer test data also performed on fully saturated samples, where κ represents the elastic compressibility in the ln p'-v plane, λ represents the slope of the virgin compression line in the ln p'-v plane, and v_1 represents the specific volume of a normally consolidated material at $p' = 1$ kPa. Numerical predictions of the clay response in oedometric compression are shown in Figure 4a for a specimen with a representative OCR = 5. In the elastic domain, the material was considered isotropic and linear, assuming a Poisson's ratio $\mu = 0.3$ and a bulk modulus, K, depending on p', v and κ.

The loading collapse (LC) yield curve of the constitutive model (Figure 7b), was considered, for simplicity, to vary linearly in the p-s_{eq} plane. The model also adopts a suction increase (SI) yield surface (Figure 7b), but this feature was not activated in the analysis because significant s_{eq} increases were not expected according to the field measurements. Instead, all the suction-induced strains were controlled by an elastic compressibility, κ_s, specifically activated only for suctions larger than the air-entry value, s_{air}. A non-linear variation of κ_s was assumed, following the expression $\kappa_s = \chi \times (S_r)^{\omega}$ proposed by Tsiampousi et al. (2013*b*), where χ and ω are fitting parameters. The air-entry value, s_{air}, was assumed to coincide with the 'gross' air-entry value of the Paola Doce clay (i.e. 1000 kPa), while the values of the parameters χ and ω were calibrated based on the results of staged unconfined drying tests during which void ratio and suction were measured (see comparison between experimental and numerical results for a representative test in Figure 8).

To complement the mechanical model, the hydraulic aspect of the clay behaviour was simulated with the van Genuchten (1980) soil water retention (SRW) model, defined in terms of degree of saturation, S_r, according to the expression

$$S_r = \left[\frac{1}{1 + (s \cdot \alpha)^n}\right]^m \cdot (1 - S_{res}) + S_{res} \quad (4)$$

© The Author(s) or their Institution(s)

where S_{res} corresponds to the residual degree of saturation, and α, n, m are fitting parameters, whose values are reported in Table 2. A comparison between the selected SWR curve and some of the laboratory data collected by Pedone (2014) is shown in Figure 6a. While the fissured Paola Doce clay has a double-porosity structure (the porosity of the intact clay between the fissures and the porosity of the fissures), it was difficult from the data in Figure 6a to distinguish the two levels and fully identify the influence of the fissures on the retentive behaviour of the material. Consequently, a unimodal water retention curve was adopted, and selected to simulate the high retention capacity exhibited by the intact clay between the fissures.

For consistency, a unimodal hydraulic conductivity model was also used, with Figure 6b showing the variation with suction of the ratio, k_r, between the current hydraulic conductivity (at current value of suction), k, and the hydraulic conductivity at full saturation, k_{sat}. This model covers both the saturated and unsaturated range of clay behaviour, and its expression is given in Equation (5), where s_{min} and s_{max} define the suction range over which the hydraulic conductivity variations take place, while k_{min} corresponds to the minimum hydraulic conductivity that the material can attain.

$$\log k = \log k_{sat} - \frac{s - s_{min}}{s_{max} - s_{min}} \log \frac{k_{sat}}{k_{min}} \quad (5)$$

The hydraulic conductivity model parameters are reported in Table 2, and were defined to have a moderate hydraulic conductivity reduction for suctions lower than 1000 kPa, the latter corresponding to the 'gross' air-entry value of the Paola Doce clay. For suctions higher than 1000 kPa, a hydraulic conductivity reduction of six orders of magnitude was assumed, which is similar to the reduction that would be estimated with a van Genuchten (1980) hydraulic conductivity model.

The saturated hydraulic conductivity, k_{sat}, was assumed to vary with depth following the trend shown in Figure 5. From the current ground level down to 40 m depth, a linear reduction from 3×10^{-8} m/s to 2×10^{-10} m/s was defined, following the in situ hydraulic conductivity measurements available. At

© The Author(s) or their Institution(s)

depths larger than 40 m below the current ground level, $k_{sat} = 2 \times 10^{-10}$ m/s was assumed. A constant hydraulic conductivity of 3×10^{-8} m/s was assigned to the material located above the current ground level, the latter removed at the beginning of the slope analysis in order to simulate river erosion processes, as described in detail in the next section. Given that this portion of the slope was only active during the first stage of the numerical simulation, the corresponding hydraulic conductivity is not shown in Figure 5, for sake of clarity.

Description of the slope numerical model

Geometry and initial conditions

The slope geometry was discretised using eight-noded isoparametric quadrilateral elements (Figure 9). All nodes were assigned two displacement degrees of freedom, while pore pressure degrees of freedom were assigned only to the corner nodes. The model was 1640 m long, and its depth ranged from 325 m (left boundary) to 136 m (right boundary), as shown in Figure 9a. For simplicity, the slope gradient was assumed constant and equal to 12.5°, which is a typical inclination of the Southern Apennines' clay slopes.

Figures 9b and 9c show the mechanical and hydraulic boundary conditions adopted during the different stages of the analysis. The lateral boundaries were restrained in the horizontal direction, while both horizontal and vertical movements were restrained at the bottom of the mesh. All boundaries, except the top one, were assumed impervious, because left and right boundaries were meant to represent the watershed of the hydrologic basin and the centre of the river valley, respectively, while the bottom boundary was set at depths where the hydraulic conductivity is extremely low. On the top boundary, a suction of 40 kPa was defined at the beginning of the analysis (Stage 0 in Table 3), which is compatible with a hydrostatic pore pressure distribution characterised by a water table depth of 4 m (typically observed in the slopes of reference towards the end of summer).

© The Author(s) or their Institution(s)

The initial vertical effective stresses were defined according to the average bulk unit weight, γ, of the Paola Doce clay, equal to 21 kN/m^3, and considering a hydrostatic pore pressure distribution complying with a 4 m deep water table. The corresponding initial horizontal stresses were defined assuming a coefficient of earth pressure at rest, K_0, equal to 1.1, based on both the OCRs of the clay and the significant lateral compression that they experienced during the orogenesis (as also observed by Tagarelli and Cotecchia 2020). Furthermore, in the central part of the model, where the ground level is sloping, non-zero initial shear stresses were defined. They were calculated assuming infinite slope conditions, for which the Mohr circles (and the corresponding poles) can be determined at each point (based on the vertical effective stresses acting on the planes parallel to the ground level and knowing the normal effective stresses acting on the horizontal and vertical planes).

An initial overconsolidation ratio R = 3.5 was assigned to the whole model. This sits towards the lower bound of the values observed for undisturbed Paola Doce clay samples, so that values close to the measured ones could be achieved after modelling river erosion, the latter simulated by excavating the area highlighted in grey in Figure 9a. ICFEP automatically calculates the initial void ratios from the initial R and p' defined, based on the material properties ν_1, λ and κ. The calculated values of the void ratio profile down the vertical T in Figure 9a are depicted by a grey broken line in Figure 3 and compare well with the laboratory measurements of void ratio distribution with depth.

Modelling river erosion

After defining the initial stress state of the slope (Stage 0 in Table 3), long-term conditions were simulated (Stage 1 in Table 3), to obtain a stress state compatible with the initial boundary conditions applied, the latter indicated in Figure 9b. Subsequently, river erosion was modelled (Stage 2 in Table 3) and long-term conditions were allowed to take place again (Stage 3 in Table 3), in order to achieve steady-state conditions compatible with the new boundary conditions applied, which are shown in Figure 9c.

© The Author(s) or their Institution(s)

The eroded area was quantified based on information gathered during a geological survey, when old alluvial deposits indicating the past location of the riverbed were logged on the slope (see Figure 2). River erosion was simulated by first removing the region highlighted in grey in Figure 9a at the beginning of Stage 2 and by replacing it with the stresses that it was inducing in the elements underneath. These stresses were then gradually reduced to zero during the 50 increments forming Stage 2, each increment lasting 50 years, so that slow river erosion processes could be simulated. As indicated in Figure 9c, throughout Stages 2 and 3, a suction of 40 kPa was assigned to the newly formed top boundary (i.e. the current ground level), except for two zones of the two horizontal top boundaries, where a pore pressure of 0 kPa was assigned in order to model the presence of a spring at the crest of the slope and a river at its toe (Figure 9c).

Modelling soil-vegetation-atmosphere interaction

After Stage 3, the mechanical and hydraulic boundary conditions were kept unchanged, except for the sloping part of the top boundary, where a 'weather boundary condition' was applied (Figure 9c), employing time steps of 5 days (Stages 4 and 5 in Table 3).

The weather boundary condition herein adopted (Smith et al. 2008) may operate either as a prescribed flow condition, by specifying a constant inflow/outflow rate, q_{nb}, or as a constant pore pressure condition, p_{fb}. At the beginning of every increment of the analysis, the pore pressure at the node where the condition is applied is compared to the prescribed value p_{fb}. If it is found to be more tensile than p_{fb}, a flow rate equal to q_{nb} is applied, otherwise a pore pressure equal to p_{fb} is imposed. The latter condition effectively means that only a proportion of the applied q_{nb} infiltrates the ground, while the rest is considered as run-off and, as it takes place outside the FE mesh, is disregarded from the analysis. It is worth observing that changes from one condition to the other can potentially occur during an increment, and not necessarily at the beginning of it. For this reason, an automatic incrementation algorithm is used in ICFEP in conjunction with the precipitation boundary condition,

© The Author(s) or their Institution(s)

so that the specified increment can be broken down into smaller sub-increments in order to apply an appropriate boundary condition, i.e. q_{nb} or p_{fb}.

In the analysis herein presented, p_{fb} was set equal to -5k Pa (i.e. a nominal 5 kPa of suction) and the inflow/outflow rates, q_{nb}, were set equal to the difference between the total rainfall (thereafter referred to as 'gross' rainfall) and the evapo-transpiration rates. The gross rainfall (Figure 10a) was that measured at the closest weather station, located in Melfi, a few kilometres from the Pisciolo slope. The evapo-transpiration rates were estimated by means of the FAO Penman-Monteith method (Allen et al. 1998), based on the average monthly temperatures recorded at the Melfi weather station (Figure 10b) and considering the presence of winter wheat, typically cultivated in Southern Italy (including the Pisciolo slope). The actual evapo-transpiration estimates were determined on a monthly basis (Figure 10c), because hourly or daily estimates would require, ideally, more frequent and accurate weather data, possibly collected by means of a weather station located directly on the slope. For similar reasons, separate estimates of evaporation and transpiration fluxes were not derived, and a unique evapo-transpiration out-flow was determined instead, following the "single crop coefficient approach" described in Allen et al. (1998). More details regarding the procedure adopted to estimate evapo-transpiration at the Pisciolo locality are extensively described in Cotecchia et al. (2014).

The stress-strain conditions achieved at the end of Stage 3 can be considered only partially representative of the current conditions of the slope, as they do not include any soil-vegetation-atmosphere interaction effects. Stage 4 was aimed at approaching stress-strain conditions closer to the current ones, and this was attained by analysing the long-term response of the slope to weather conditions typically encountered in South of Italy. To this extent, a 'typical' year of weather was derived from data recorded between 1 September 2006 and 31 August 2007 at the Melfi weather station (Figure 10) and applied in the analysis 20 consecutive times, as reported in Table 3. This year of weather was identified as 'representative' as it was neither too dry in spring and summer, nor too rainy in autumn and winter, compared to other recent years for which weather data were measured at

© The Author(s) or their Institution(s)

the Melfi weather station. When comparing the weather data that became available, the raininess of each year was evaluated based on the total annual rainfall recorded (around 765 mm from 1 September 2006 to 31 August 2007), while its dryness was judged based on the total annual evapo-transpiration estimated following the FAO Penman-Monteith method (around 270 mm from 1 September 2006 to 31 August 2007).

Stage 4 therefore resulted in stress-strain conditions in the slope representative of the current ones, hence serving as a process of initialisation of stresses and strains for Stage 5, when the response of the slope to a recent weather history was investigated. The weather boundary condition applied in Stage 5 (Figure 9c) was derived from the weather data recorded in Melfi between 1 September 2007 and 31 August 2012 (Figure 10), when the monitoring data at Pisciolo were collected.

Discussion of the results

Effects of river erosion

Draft

After modelling river erosion, significant upward movements (almost 1.5 m) were observed at the toe of the slope. This is shown in Figure 11a, where the vectors of the displacements mobilised between the end of Stage 1 and the end of Stage 3 (Table 3) are plotted with reference to the toe area of the slope indicated in Figure 9a. The movements predicted in this zone are associated with large deviatoric plastic strains (more than 10%), whose contours, shown in Figure 12a, indicate a shear band that starts to form from the toe. The deviatoric strains herein referred to, defined as E_d, correspond to the generalised ones, expressed as

$$E_d = \frac{2}{\sqrt{6}}\sqrt{(\varepsilon_x - \varepsilon_y)^2 + (\varepsilon_y - \varepsilon_z)^2 + (\varepsilon_z - \varepsilon_x)^2 + \gamma_{xy}^2 + \gamma_{xz}^2 + \gamma_{yz}^2} \quad (6)$$

Due to river erosion, the void ratio increased in the lower part of the slope, becoming even closer to the one measured on undisturbed specimens. This is shown with a solid line in Figure 3, where the distributions of void ratio with depth are plotted with reference to the vertical T in Figure 9a. The

© The Author(s) or their Institution(s)

slope appeared to be globally stable at the end of Stage 3, having a factor of safety close to 1.3, calculated according to the numerical approach implemented in ICFEP by Potts and Zdravkovic (2012).

Long-term effects of 'typical' weather conditions

The pore pressure variations predicted, during Stage 4 (Table 3), at 0 m, 15 m and 36 m deep points (along the vertical P in Figure 9a) are illustrated in Figure 13 (note that the start of each year on the time axis is in September). At ground level (Figure 13a), the highest suctions, around 80 kPa, were predicted between the end of spring and the end of summer, while the minimum prescribed suction, of 5 kPa, occurred, every year, during the wettest seasons, indicating potential run-off taking place. At 15 m depth (Figure 13b), pore pressure variations of around 30 kPa, similar to those measured on site (Figure 1), were estimated. Furthermore, as often observed in the Southern Apennines at intermediate depths (i.e. 10-30 m depth), the maximum and minimum pore pressures were predicted at the end of winter/early spring and at the end of summer/early autumn, respectively. The pore pressures at larger depths (see Figure 13c for pore pressures at 36 m depth) did not show significant variations within the same year, even though their average value slightly increased with time, eventually becoming constant after a few years.

When applying the 'typical' weather for 20 years, the horizontal displacements at the toe of the slope gradually increased, as a result of the rainfall infiltration occurring, each year, during the wettest months, when the pore pressures cyclically became higher than the average values attained at the end of Stage 3. As an example, Figure 13d shows the horizontal displacements mobilised, during Stage 4 only, at ground level (at the location of the vertical D in Figure 9a). In the first year, a displacement increment of almost 120 mm was observed, but afterwards it reduced to smaller rates, increasing to about 200 mm after 10-15 years, until no significant displacement variations could be observed. Within each year, the displacements increased between early autumn and early spring, while small displacement reductions were predicted until the end of summer, as a result of a shrinkage associated

© The Author(s) or their Institution(s)

with the pore pressure reductions previously discussed. The results in Figure 13 would suggest that a long-term hydro-mechanical balance could be achieved if the slope is affected by the same seasonal variations in weather every year. However, this is unlikely to be the case if permanent deformations induced by cyclic hydraulic loading are modelled (e.g. adopting a model that would simulate plasticity from an early stage of a loading path, like the models proposed by Rouania and Muir Wood 2000, or Grammatikopoulou et al. 2008).

The vectors of the movements predicted during Stage 4 only are reported in Figure 11b. They show the extent of the landslide body (around 25 m deep and 125 m long) mobilised at the end of Stage 4 as a consequence of the slope being subjected to 20 years of 'typical' weather conditions. The corresponding contours of the deviatoric plastic strains mobilised since the start of Stage 4 are reported in Figure 12b, indicating a further progression of the shear band up the slope. These results demonstrate that this is clearly a progressive phenomenon and highlight the importance of adequately modelling the history of a natural slope, even when the analysis is intended to study only soil-vegetation-atmosphere interaction effects.

Draft

Effects of recent weather history

The weather observed between 1 September 2007 and 31 August 2012 (Figure 10) was simulated during Stage 5 (see Table 3 and Figure 9c). Although the analysis did not attempt to reproduce the exact events that took place at Pisciolo, qualitative comparisons with the monitoring data from Pisciolo provides evidence as to how representative the analysis is of the conditions encountered on the Southern Apennines' clay slopes (with particular reference to the weather conditions, which are broadly representative of the Mediterranean region; Peel et al. 2007).

The predicted trend of the superficial suction changes (Figure 14a) is entirely consistent with the measured rainfall and evapo-transpiration balance over the recorded period (Figure 10). Large suctions (up to around 250 kPa) are mobilised during spring in each of the years 2007 to 2010, when

© The Author(s) or their Institution(s)

higher evapo-transpiration rates are estimated (Figure 10c). These large suctions tend to dissipate towards the end of summer, when the wet seasons are approaching and a more regular rainfall infiltration takes place (Figure 10a). The significant rainfall events at the start of the dry seasons in 2011 and 2012 (Figure 10a), together with reduced evapotranspiration rates (Figure 10c), contributes to much reduced suctions predicted in these two years.

As shown in Figure 14a, the suctions predicted at ground level tend to be lower than those measured on samples collected at shallow depths at Pisciolo (up to 1.5 m depth in the area indicated as S in Figure 2). The difference between measured and predicted values of suction could be attributed to the applied model calibration, which was shown, in Figure 8, to under-predict suctions lower than 1 MPa. It is possible that more accurate suction variations could be obtained by employing water retention and hydraulic conductivity models capable of simulating more closely the effects that a double-porosity structure might have on the hydraulic response of a fissured material. Moreover, it is worth noting that the presence of desiccation cracks, extensively observed by Pedone (2014) at Pisciolo, was not simulated in the analysis. Therefore, the effects of the evaporation processes taking place within the cracks were neglected, and this could also represent a reason why suctions at very shallow depths were underestimated during the slope analysis.

The pore pressure variations predicted at 15 m depth are reported in Figure 14b in comparison with the pore pressures measured at Pisciolo between 13 m and 15 m depth (see Figure 2 for piezometer locations). It is interesting to observe that, even at this depth, the predicted variation follows the pattern of applied weather boundary conditions. It is also encouraging that predicted pore pressure magnitudes agree reasonably well, on average, with the available measurements, although the latter exhibit smaller seasonal fluctuations.

The predicted pore pressures at 36 m depth (Figure 14c) indicate that the seasonal variations of the weather boundary conditions at the surface no longer induce significant pore pressure fluctuations at large depths. However, the monitoring data collected at Pisciolo between 33 m and 36 m depth (see

© The Author(s) or their Institution(s)

Figure 2 for piezometer locations) still show some seasonal changes, but their average magnitude agrees very well with the values predicted (Figure 14c). These results confirm findings by Pedone et al. (2018) with reference to a uniform clay slope, in that significant pore pressure fluctuations at large depths can probably occur only if highly permeable inclusions are interbedded within the clays, which were not considered in the current numerical model.

An overall increase in the horizontal displacements was predicted at the toe of the slope at ground surface during Stage 5, as shown in Figure 14d (with reference to the vertical D in Figure 9a, which broadly coincides with inclinometer I12 in Figure 2). As already noted for Stage 4, the displacements increased in the months of the highest rainfall, and reduced, due to soil shrinkage, in the driest and warmest months. Consistent with the previous discussion regarding the information reported in Figure 14a, it is interesting to observe that, between 2007 and 2010, the average displacement remained broadly constant, while in 2011 and 2012, when the climate was wetter and with lower evapo-transpiration (Figure 10), the average displacement increased by about 15 mm, as a results of an average increase in pore pressures due to higher rainfall infiltration.

The displacement vectors around the slope toe (Figure 9a), mobilised in the period 1 September 2007 – 31 August 2012 (i.e. during Stage 5 in Table 3), are shown in Figure 11c, while the corresponding contours of the deviatoric plastic strains mobilised between the end of Stage 4 and the end of Stage 5 are illustrated in Figure 12c. Both figures clearly indicate further mobilisation of the landslide body already formed during Stage 4, with the shear band progressing from the toe to about 125 m up the slope. As previously mentioned, further straining accumulated during Stage 5 due to an average increase in pore pressures, the latter mainly observed when modelling the weather conditions recorded in 2011 and 2012.

The profiles of horizontal displacements along the vertical D (Figure 9a) are plotted in Figure 15. The horizontal displacements mobilised between the end of Stage 3 and the end of Stage 4 (Table 3) are shown with a bold continuous line, while those gradually accumulating during the subsequent Stage

© The Author(s) or their Institution(s)

5 (i.e. during the period 1 September 2007 – 31 August 2012) are shown, at intervals of 3 months, with thinner dashed lines. The last inclinometer reading collected at Pisciolo through inclinometer I12 (Figure 2) is also plotted in Figure 15 (dashed bold grey line).

The depth of the shear band predicted by the analysis, of around 25 m, is similar to the one observed at Pisciolo, therefore reasonably representing the first mobilisation of the landslide body C9 (Figure 2). This suggests that, for a slope with hydro-mechanical properties similar to those characterising the fissured clay slopes of the Southern Apennines, soil-vegetation-atmosphere interaction is capable of promoting the gradual formation of a landslide mechanism at depths as large as 25 m.

Conclusions

The paper presents a two-dimensional plane strain hydro-mechanically coupled finite element analysis of a natural slope representative of a class of slopes located in the Southern Apennines. The numerical model, developed with the finite element code ICFEP, employed a constitutive model capable of simulating the behaviour of highly overconsolidated clays in both saturated and unsaturated conditions, in conjunction with advanced hydraulic boundary conditions that enabled realistic inclusion of weather events in the investigation of the slope response with time.

The mechanical model, together with the water retention and hydraulic conductivity models, was calibrated on the case study of the Pisciolo slope, for which extensive laboratory and site investigation was performed, together with the monitoring of ground movements and pore pressures, the latter carried out between 2009 and 2012. The weather boundary conditions were defined from the weather data collected at the Melfi weather station, located in the proximity of the Pisciolo slope, where seasonal variations typical of the Southern Apennines (and, more generally, of the Mediterranean region) were recorded.

The present work reveals the importance of reproducing adequately the geological history of a natural slope to its current state, even when the analysis is intended to study only soil-vegetation-atmosphere

© The Author(s) or their Institution(s)

interaction effects. For the Pisciolo case study, the first-time failure observed at the toe of the slope, also predicted in the analysis herein presented, most likely started forming from a zone where shear strains initially accumulated due to soil erosion processes.

The proposed modelling strategy is demonstrated to capture very well the overall hydraulic response of the slope to soil-vegetation-atmosphere interaction. The suction variations estimated at shallow depths are shown to follow reasonably well the weather variations acting at ground level, even though the suction magnitude was underestimated at the peak of the driest season. The pore pressure variations predicted at intermediate depths (e.g. 15 m depth) are very similar to those recorded at Pisciolo and in other slopes located in the Southern Apennines (e.g. the Pianello slope; Figure 1). The numerical model reproduced well also the pore pressure values at large depths (e.g. 36 m depth), but their fluctuations with time were underestimated. This is probably due to the fact that the highly permeable inclusions, recurrently observed within the turbiditic units forming the Southern Apennines' slopes, were not modelled in the analysis.

The order of magnitude of the displacements induced in the analysis by soil-vegetation-atmosphere interaction phenomena is very similar to the one often observed for the clay slopes of the Southern Apennines, including the Pisciolo slope. The accurate prediction of these displacements is of significant importance for quantifying landslide risk in areas like Southern Italy, where slope stability issues constantly cause material and human losses. To this aim, the modelling strategy described in the paper could be used as a template for investigating the effects of future climate scenarios on the stability of highly overconsolidated clay slopes. Employing a constitutive model with a smooth transition between saturated and unsaturated soil states, as in the current study of the Pisciolo slope, would enable the investigation of more extreme climate scenarios that could potentially induce larger suctions at shallow depths.

Acknowledgements

© The Author(s) or their Institution(s)

The authors would like to thank the Apulian Aqueduct Spa for their financial and technical support. They also would like to express their gratitude to researches and technicians of Technical University of Bari, CNR-IRPI of Bari and Imperial College London for having provided key data and facilities for ICFEP analyses, respectively. Matteo Pugliese is finally acknowledged for the essential support in performing the in situ hydraulic conductivity measurements used in the analysis.

Draft

© The Author(s) or their Institution(s)

References

Allen, R.G., Pereira, L.S., Raes, D., and Smith, M. 1998. Crop evapo-transpiration (guidelines for computing crop water requirements). FAO Irrigation and Drainage Paper No. 56.

Alonso, E.E., Gens, A., and Josa, A. 1990. A constitutive model for partially saturated soils. Géotechnique, **40**(3): 405-430.

Askarinejad, A., Akca, D., and Springman S.M. 2018. Precursors of instability in a natural slope due to rainfall: a full-scale experiment. Landslides, **15**(15): 1745-1759.

Biot, M.A. 1941. General theory of three-dimensional consolidation. Journal of Applied Physics, **12**: 155-164.

Blight, G.E. 1997. Interactions between the atmosphere and the Earth. Géotechnique, **47**(4): 713-767.

Cafaro, F., and Cotecchia, F. 2015. Influence of the mechanical properties of consolidated clays on their water retention curve. Italian Geotechnical Journal, **2**: 13-29.

Capobianco, V., Cascini, L., Cuomo, S., and Foresta, V. 2020. Wetting-drying response of an unsaturated pyroclastic soil vegetated with long-root grass. Environmental Geotechnics, Ahead of print, doi: 10.1680/jenge.19.00207.

Cascini, L., Calvello, M., and Grimaldi, G.M. 2010. Groundwater modeling for the analysis of active slow-moving landslides. Journal of Geotechnical and Geoenvironmental Engineering, **136**(9): 1220-1230.

Cotecchia, F., Pedone, G., Bottiglieri, O., Santaloia, F., and Vitone, C. 2014. Slope-atmosphere interaction in a tectonized clayey slope: a case study. Italian Geotechnical Journal, **1**: 34-61.

Draft

© The Author(s) or their Institution(s)

Cotecchia, F., Vitone, C., Santaloia, F., Pedone, G., and Bottiglieri, O. 2015. Slope instability processes in intensely fissured clays: case histories in the Southern Apennines. Landslides, **12**: 877-893.

Cotecchia, F., Santaloia, F., Lollino, P., Vitone, C., Pedone, G., and Bottiglieri, O. 2016. From a phenomenological to a geomechanical approach to landslide hazard analysis. European Journal of Environmental and Civil Engineering, **20**(9): 1004-1031.

Davies, O., Rouania, M., Glendinning, S., Cash, M., and Trento, V. 2014. Investigation of a pore pressure driven slope failure using a coupled hydro-mechanical model. Engineering Geology, **178**: 70-81.Elia, G., Cotecchia, F., Pedone, G., Vaunat, J., Vardon P.J., Pereira, C., Springman, S.M., Rouania, M., Van Esch, J., Koda, E., Josifovski, J., Nocilla, A., Askarinejad, A., Stirling, R., Helm, P., Lollino, P., and Osinski, P. 2017. Numerical modelling of slope-vegetation-atmosphere interaction: an overview. Quarterly Journal of Engineering Geology and Hydrogeology, **50**: 249-270.

Gens, A. 2010. Soil-environment interactions in geotechnical engineering. Géotechnique, **60**(1): 3-74.

Georgiadis, K., Potts D.M., and Zdravkovic, L. 2005. Three-dimensional constitutive model for partially and fully saturated soils. International Journal of Geomechanics, **5**(3): 244-255.

Grammatikopoulou, A., Zdravkovic, L., and Potts, D.M. 2008. The influence of previous stress history and stress path direction on the surface settlement trough induced by tunnelling. Géotechnique, **58**(4): 269-281.

Hungr, O., Leroueil, S., and Picarelli, L. 2014. The Varnes classification of landslide types, an update. Landslides, **11**: 167-194.

Kenney, T.C., and Lau, K.C. 1984. Temporal changes of groundwater pressure in a natural slope of non fissured clay. Canadian Geotechnical Journal, **21**(1): 138-146.

© The Author(s) or their Institution(s)

Draft

Kovacevic, K., Potts, D.M., and Vaughan, P.R. 2001. Progressive failure in clay embankments due to seasonal climate changes. *In* Proceedings of the 5th International Conference of Soil Mechanics and Geotechnical Engineering, Istanbul, Turkey, vol. 3, pp. 2127-2130.

Lagioia, R., Puzrin, A.M., and Potts, D.M. 1996. A new versatile expression for yield and plastic potential surfaces. Computers and Geotechnics, **19**(3): 171-191.

Leroueil, S. 2001. Natural slopes and cuts: movement and failure mechanisms. Géotechnique, **51**(3): 197-243.

Lollino, P., Cotecchia, F., Elia, G., Mitaritonna, G., and Santaloia, F. 2016. Interpretation of landslide mechanisms based on numerical modelling: two case-histories. European Journal of Environmental and Civil Engineering, **20**(9): 1032-1053.

Marinho, F.A.M., and Oliveira, O.M. 2006. The filter paper method revisited. Geotechnical Testing Journal, **29**(3): 250-258.

Matsuoka, H., and Nakai, T. 1974. Stress-deformation and strength characteristics of soil under three different principal stresses Proceedings of Japan Society of Civil Engineers, **232**: 59–70.

Nyambayo, V.P., and Potts D.M. 2010. Numerical simulation of evapotranspiration using a root water uptake model. Computers and Geotechnics, **37**(1-2): 175-186.

Palmisano, F., Vitone, C., and Cotecchia, F. 2018. Assessment of landslide damage to buildings at the urban scale. Journal of Performance of Constructed Facilities, **32**(4): 04018055-(1-13).

Pedone, G. 2014. Interpretation of slow and deep landslides triggered by slope-atmosphere interaction in slopes formed of fissured clayey turbidites. Ph.D. thesis, Technical University of Bari, Bari, Italy.

Pedone, G., Ruggieri, G., and Trizzino, R. 2018. Characterisation of climatic variables used to identify instability thresholds in clay slopes. Géotechnique letters, **8**(3): 231-239.

Draft

© The Author(s) or their Institution(s)

Peel, M.C., Finlayson, B.L., and McMahon T.A. 2007. Updated world map of the Koppen-Geiger climate classification. Hydrology and Earth System Sciences, **11**: 1633-1644.

Pirone, M., Damiano, E., Picarelli, L., Olivares, L., and Urciuoli, G. 2012. Groundwater-atmosphere interaction in unsaturated pyroclastic slopes at two sites in Italy. Italian Geotechnical Journal, **3**: 29-49.

Pirone, M., Papa, R., Nicotera, M.V., and Urciuoli, G. 2015. In situ monitoring of the groundwater field in an unsaturated pyroclastic slope for slope stability evaluation. Landslides, **12**: 259-276.

Potts, D.M., and Ganendra, D. 1994. An evaluation of substepping and implicit stress point algorithms. Computer Methods in Applied Mechanics and Engineering, **119**(3-4): 341-354.

Potts, D.M., and Zdravkovic, L. 1999. Finite element analysis in geotechnical engineering: theory. Thomas Telford, London.

Potts, D.M., and Zdravkovic, L. 2012. Accounting for partial material factors in numerical analysis. Géotechnique, **62**(12): 1053-1065.

Ridley, A.M., and Burland, J.B. 1993. A new instrument for the measurement of soil moisture suction. Géotechnique, **43**(2): 321-324.

Rouania, M., and Muir Wood, D. 2000. A kinematic hardening constitutive model for natural clays with loss of structure. Géotechnique, **50**(2): 153-164.

Rouania, M., Helm, P., Davies, O., and Glendinning S. 2020. Deterioration of an infrastructure cutting subjected to climate change. Acta Geotechnica, **15**: 2997-3016.Sitarenios, P., Casini, F., Askarinejad, A., and Springman S.M. 2019. Hydro-mechanical analysis of a surficial landslide triggered by artificial rainfall: the Ruedlingen field experiment. Géotechnique, Ahead of Print, doi: 10.1680/jgeot.18.P.188.

Draft

© The Author(s) or their Institution(s)

Smethurst, J.A., Clarke, D., and Powrie W. 2012. Factors controlling the seasonal variation in soil water content and pore water pressures within a lightly vegetated clay slope. Géotechnique, **62**(5):429-446.

Smith, P.G. 2003. Numerical analysis of infiltration into partially saturated soil slopes. Ph.D. Thesis, Imperial College London, London, UK.

Smith, P.G., Potts D.M., and Addenbrooke T.I. 2008. A precipitation boundary condition for finite element analysis. *In* Proceedings of the 1st European Conference on Unsaturated Soils, Durham, UK, pp. 773-778.

Stirling, R.A., Toll, D.G., Glendinning, S., Helm, P.R., Yildiz, A., Hughes, P.N., and Asquith, J.D. 2020. Weather-driven deterioration processes affecting the performance of embankment slopes. Géotechnique, Ahead of print, doi: 10.1680/jgeot.19.SiP.038.

Switala, B.M., and Wu W. 2018. Numerical modelling of rainfall-induced instability of vegetated slopes. Géotechnique, **68**(6):481-491.

Tagarelli, V., and Cotecchia, F. 2020. The effects of slope initialization on the numerical model predictions of the slope-vegetation-atmosphere interaction. Geosciences, **10**(85): 1-24.

Take, W.A., and Bolton, M.D. 2011. Seasonal ratcheting and softening in clay slopes, leading to first-time failure. Géotechnique, **61**(9): 757-769.

Toll, D.G., Lourenço, S.D.N., Mendes, J., Gallipoli, D., Evans, F.D., Augarde, C.E., Cui, Y.J., Tang, A.M., Rojas, J.C., Pagano, L., Mancuso, C., Zingariello, C., and Tarantino, A. 2011. Soil suction monitoring for landslides and slopes. Quarterly Journal of Engineering Geology and Hydrogeology, **44**: 23-33.

Draft

© The Author(s) or their Institution(s)

Tommasi, P., Boldini, D., Caldarini, G., and Coli, N. 2013. Influence of infiltration on the periodic re-activation of slow movements in an overconsolidated clay slope. Canadian Geotechnical Journal, **50**(1): 54-67.

Tsiampousi, A., Zdravkovic, L., and Potts, D.M. 2013*a*. A new Hvorslev surface for critical state type unsaturated and saturated constitutive models. Computers and Geotechnics, **48**: 156-166.

Tsiampousi, A., Zdravkovic, L., and Potts, D.M. 2013*b*. A three-dimensional hysteretic soil-water retention curve. Géotechnique, **63**(2): 155-164.

Tsiampousi, A., Zdravkovic, L., and Potts, D.M. 2017*a*. Numerical study of the effect of soil–atmosphere interaction on the stability and serviceability of cut slopes in London clay. Canadian Geotechnical Journal, **54**: 405-418.

Tsiampousi, A., Smith, P.G., and Potts, D.M. 2017*b*. Coupled consolidation in unsaturated soils: An alternative approach to deriving the Governing Equations. Computers and Geotechnics, **84**: 238-255.

van Genuchten, M.T. 1980. A closed form equation for predicting the hydraulic conductivity of unsaturated soils. Soil Science Society of America Journal, **44**: 892-898.

Vassallo, R., Grimaldi, G.M., and Di Maio, C. 2015. Pore water pressures induced by historical rain series in a clayey landslide: 3D modeling. Landslides, **12**: 731–744.

Vaughan, P. R. 1994. Assumption, prediction and reality in geotechnical engineering. Géotechnique, **44**(4): 573-609.

Vitone, C., and Cotecchia, F. 2011. The influence of intense fissuring on the mechanical behaviour of clays. Géotechnique, **61**(12): 1003-1018.

Draft

© The Author(s) or their Institution(s)

Vitone, C., Cotecchia, F., Viggiani, G., and Hall, S.A. 2013a. Strain fields and mechanical response of a highly to medium fissured bentonite clay. International Journal for Numerical and Analytical Methods in Geomechanics, **37**(11): 1510-1534.

Vitone, C., Viggiani, G., Cotecchia, F., and Hall, S.A. 2013b. Localized deformation in intensely fissured clays studied by 2D digital image correlation. Acta Geotechnica, **8**: 247-263.

Woodman, N.D., Smethrust, J.A., Roose, T., Powrie, W., Meijer, G.J., Knappett, J.A., and Dias, T. 2020. Mathematical and computational modelling of vegetated soil incorporating hydraulically-driven finite strain deformation. Computers and Geotechnics, **127**(103754): 1-12.

Zdravkovic, L., Tsiampousi, A., and Potts, D.M. 2018. On the modelling of soil-atmosphere interaction in cut and natural slopes. *In* Proceedings of the 7th International Conference on Unsaturated Soils, Hong Kong.

Draft

© The Author(s) or their Institution(s)

List of symbols

c' effective cohesion intercept

c'_{peak} effective cohesion intercept at peak

E_d generalised deviatoric strain

e void ratio

FE finite element

J generalised deviatoric stress invariant

J_{CS} generalised deviatoric stress invariant at critical state

K bulk modulus

K_{min} minimum bulk modulus

K_0 coefficient of earth pressure at rest

k current hydraulic conductivity

k_{min} minimum hydraulic conductivity

k_r relative hydraulic conductivity

k_{sat} saturated hydraulic conductivity

LC loading collapse yield curve

M_f constitutive model parameter for the yield function

M_g constitutive model parameter corresponding to the critical state line gradient in the p-q plane

m parameter for van Genuchten (1980) model

Draft

© The Author(s) or their Institution(s)

m_{HV} constitutive model parameter for the plastic potential on the dry side

n parameter for van Genuchten (1980) model

n_{HV} constitutive model parameter for the yield surface on the dry side

OCR overconsolidation ratio defined as σ'_{vy}/σ'_{v}

p equivalent mean stress

p' mean effective stress

p'_{y} mean effective stress at yield

p_{CS} mean stress at critical state

p_{fb} pore water pressure prescribed with the weather boundary condition

p_{0} equivalent mean stress at yield

PP plastic potential

q deviatoric triaxial stress

q_{nb} flow prescribed with the weather boundary condition

R overconsolidation ratio defined as p'_{y}/p'

s matrix suction

s_{air} air-entry value

s_{eq} equivalent suction

s_{min} parameter for hydraulic conductivity model

s_{max} parameter for hydraulic conductivity model

Draft

© The Author(s) or their Institution(s)

s_0 matrix suction at yield

S_r degree of saturation

S_{res} residual degree of saturation

SI suction induced yield surface

t time

u pore water pressure

u_a pore air pressure

YS yield surface

α parameter for van Genuchten (1980) model

α_f constitutive model parameter for the yield surface on the wet side

α_g constitutive model parameter for the plastic potential on the wet side

α_{HV} constitutive model parameter for the yield surface on the dry side

β_{HV} constitutive model parameter for the plastic potential on the dry side

γ bulk unit weight of the soil

χ fitting parameter for κ_s calculation

ε_s total deviatoric strain

φ' effective angle of shear resistance

φ'_{peak} effective angle of shear resistance at peak

κ elastic compressibility coefficient related to mean stress variations

Draft

© The Author(s) or their Institution(s)

κ_s elastic compressibility coefficient related to suction variations for $s_{eq} > 0$

λ compressibility coefficient for virgin soil states related to mean stress variations

μ_f constitutive model parameter for the yield surface on the wet side

μ_g constitutive model parameter for the plastic potential on the wet side

μ Poisson's ratio

σ_{tot} total stress

σ' effective stress

σ_{eq} equivalent stress

σ_{net} net stress

σ'_v vertical effective stress

σ'_{vy} vertical effective stress at yield

ν specific volume

ν_1 specific volume at p' = 1 kPa

ω fitting parameter for κ_s calculation

Draft

© The Author(s) or their Institution(s)

Table 1. Constitutive model parameters adopted in the slope analysis.

Parameter	**Symbol**	**Value**
Poisson's ratio	μ [-]	0.3
Minimum bulk modulus	K_{min} [kPa]	8000.0
Specific volume at p' = 1kPa	v_1 [-]	2.243
Virgin compression line slope	λ [-]	0.0914
Swelling line slope	κ [-]	0.0365

Parameter	**Symbol**	**Value**
Yield function and plastic potential parameters (wet of critical state)	$\alpha_{f,g}$ [-]	0.25
	$\mu_{f,g}$ [-]	0.65
	$M_{f,g}$ [-]	0.689*
Yield function parameters (dry of critical state)	α_{HV} [-]	0.3
	n_{HV} [-]	0.45
Plastic potential parameters (dry of critical state)	β_{HV} [-]	0.2
	m_{HV} [-]	1.5

* M_g = 0.689 corresponds to φ' = 18° in triaxial compression.

Parameter	**Symbol**	**Value**
Pore air pressure	u_a [kPa]	0.0
Air-entry value	s_{air} [kPa]	1000.0
Parameters for elastic compressibility coefficient for $s_{eq} > 0$	χ [-]	0.6
	ω [-]	8.0

Draft

© The Author(s) or their Institution(s)

Table 2. Water retention and hydraulic conductivity model parameters adopted in the slope analysis.

Parameter	Symbol	Value
Water retention model parameters	S_{res} [%]	5.0
	α [1/kPa]	0.00055
	n [-]	1.15
	m [-]	0.35
Hydraulic conductivity model parameters	s_{min} [kPa]	100.0
	s_{max} [kPa]	10000.0
	k_{sat} [m/s]	Depth-dependent (see Figure 5)
	k_{sat}/k_{min} [-]	10^6

Draft

© The Author(s) or their Institution(s)

Table 3. Main stages of the slope analysis.

Stage number	Key processes modelled	Increment number	Increment size	Total stage duration
0	Set up initial conditions	-	-	-
1	Long-term conditions	1 - 50	Variable	4000 years
2	River erosion processes	51 - 100	50 years	2500 years
3	Long-term conditions	101 - 150	Variable	4000 years
4	'Typical' climatic conditions (1 Sep. 2006 – 31 Aug. 2007)	151 - 1610	5 days	20 years
5	Recent climatic history (1 Sep. 2007 – 31 Aug. 2012)	1611 - 1976	5 days	5 years

Draft

© The Author(s) or their Institution(s)

Figure captions

Figure 1. Monitoring data of the Pisciolo slope (a), located in Basilicata region (Italy), and the Pianello slope (b), located in Apulia region (Italy) (modified from Cotecchia et al. 2014).

Figure 2. Geological map (a) and section (b) of the Pisciolo slope. Key: (1) fan deposit; (2) debris deposit; (3) alluvial deposit; (4) Pliocene succession; (5) Numidian Flysch Formation; (6) Paola Doce Formation; (7) Red Flysch Formation; (8) Fractured rock blocks and coarse inclusions; (9) fault; (10) anticline axis; (11) landslide body (b) and corresponding crown (c) (grey line when inactive); (12) P: boreholes equipped with piezometers; G: GPS antenna; I: boreholes equipped with inclinometers; S: area of shallow sampling; (13) section in plan (modified from Cotecchia et al. 2014).

Figure 3. Void ratios measured on Paola Doce clay samples taken at Pisciolo at different depths compared with values predicted at key stages of the analysis (Table 3) along vertical T (Figure 9a).

Figure 4. Comparison between experimental and numerical results for an oedometer test (a) and a triaxial test (b and c) conducted on Paola Doce clay samples taken at Pisciolo.

Figure 5. Saturated hydraulic conductivity profile assumed in the slope analysis compared with in situ measurements conducted at Pisciolo and saturated hydraulic conductivities estimated during oedometer tests carried out on Paola Doce clay samples taken at Pisciolo.

Figure 6. Water retention data measured on Paola Doce clay samples taken at Pisciolo at shallow depths (area S in Figure 2) compared with the water retention curve used in the analysis (a) and the corresponding hydraulic conductivity function adopted (b).

Figure 7. Yield surface (YS) and plastic potential (PP) of the constitutive model adopted in the analysis reported in the p-J (a) and p-s_{eq} (b) planes.

Draft

© The Author(s) or their Institution(s)

Figure 8. Variations of void ratio (a) and suction (b) with time for an unconfined drying test conducted on a Paola Doce clay sample taken at Pisciolo: comparison between experimental and numerical results.

Figure 9. Geometry and dimensions of the slope analysed (a); mesh generated and boundary conditions adopted during Stage 1 (b) and Stages 2 to 5 (c).

Figure 10. Gross daily rainfall (a) and average monthly temperature (b) measured at the Melfi weather station; average monthly actual evapo-transpiration estimated with the FAO Penman-Monteith method (Allen et al. 1998) (c).

Figure 11. Displacements predicted: after modelling river erosion (a) (i.e. between end of Stage 1 and end of Stage 3); during Stage 4 only (b) (i.e. after simulating for 20 years the weather conditions recorded between 1 September 2006 and 31 August 2007); during Stage 5 only (c) (i.e. as a result of the weather conditions recorded between 1 September 2007 and 31 August 2012).

Figure 12. Contours of generalised deviatoric plastic strains predicted: after modelling river erosion (a) (i.e. between end of Stage 1 and end of Stage 3); during Stage 4 only (b) (i.e. after simulating for 20 years the weather conditions recorded between 1 September 2006 and 31 August 2007); during Stage 5 only (c) (i.e. as a result of the weather conditions recorded between 1 September 2007 and 31 August 2012).

Figure 13. Pore water pressure variations predicted at 0 m (a), 15 m (b) and 36 m (c) depth along vertical P (Figure 9a) and horizontal displacement variations predicted at ground level (d) along vertical D (Figure 9a) as a result of a 'typical' year of weather (i.e. 1 September 2006-31 August 2007) assumed to act 20 consecutive times (Stage 4 in Table 3).

Figure 14. Pore water pressure variations predicted at 0 m (a), 15 m (b) and 36 m (c) depth along vertical P (Figure 9a) as a result of the weather conditions recorded between 1 September 2007 and 31 August 2012 compared with pore pressures measured at 1.0-1.5 m depth (a), 13-15 m depth (b)

© The Author(s) or their Institution(s)

and 33-36 m depth (c); horizontal displacements predicted at ground level (d) along vertical D (Figure 9a) as a result of the weather conditions recorded between 1 September 2007 and 31 August 2012.

Figure 15. Profiles of horizontal displacements predicted along vertical D (Figure 9a) compared with the last inclinometer reading collected at Pisciolo through inclinometer I12 (Figure 2).

Draft

© The Author(s) or their Institution(s)

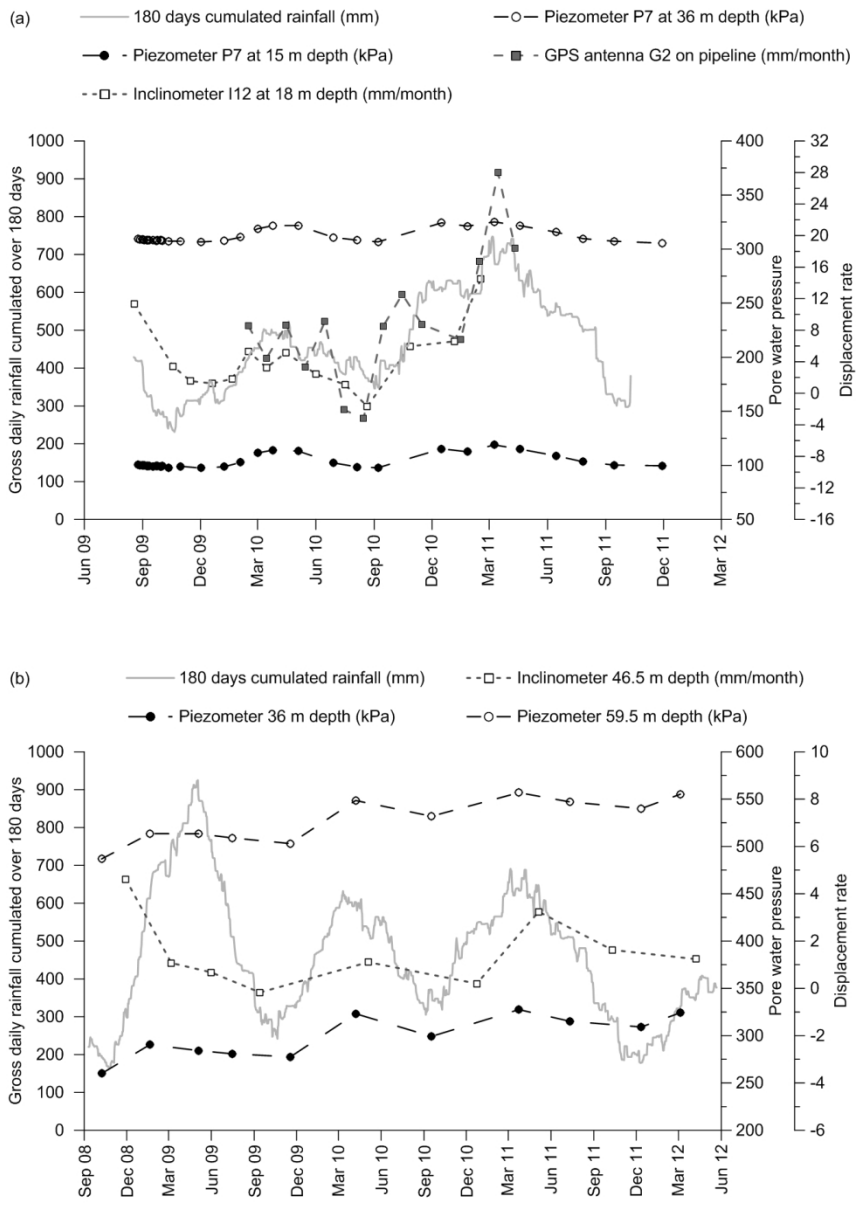


Figure 1. Monitoring data of the Pisciolo slope (a), located in Basilicata region (Italy), and the Pianello slope (b), located in Apulia region (Italy) (modified from Cotecchia et al. 2014).

© The Author(s) or their Institution(s)

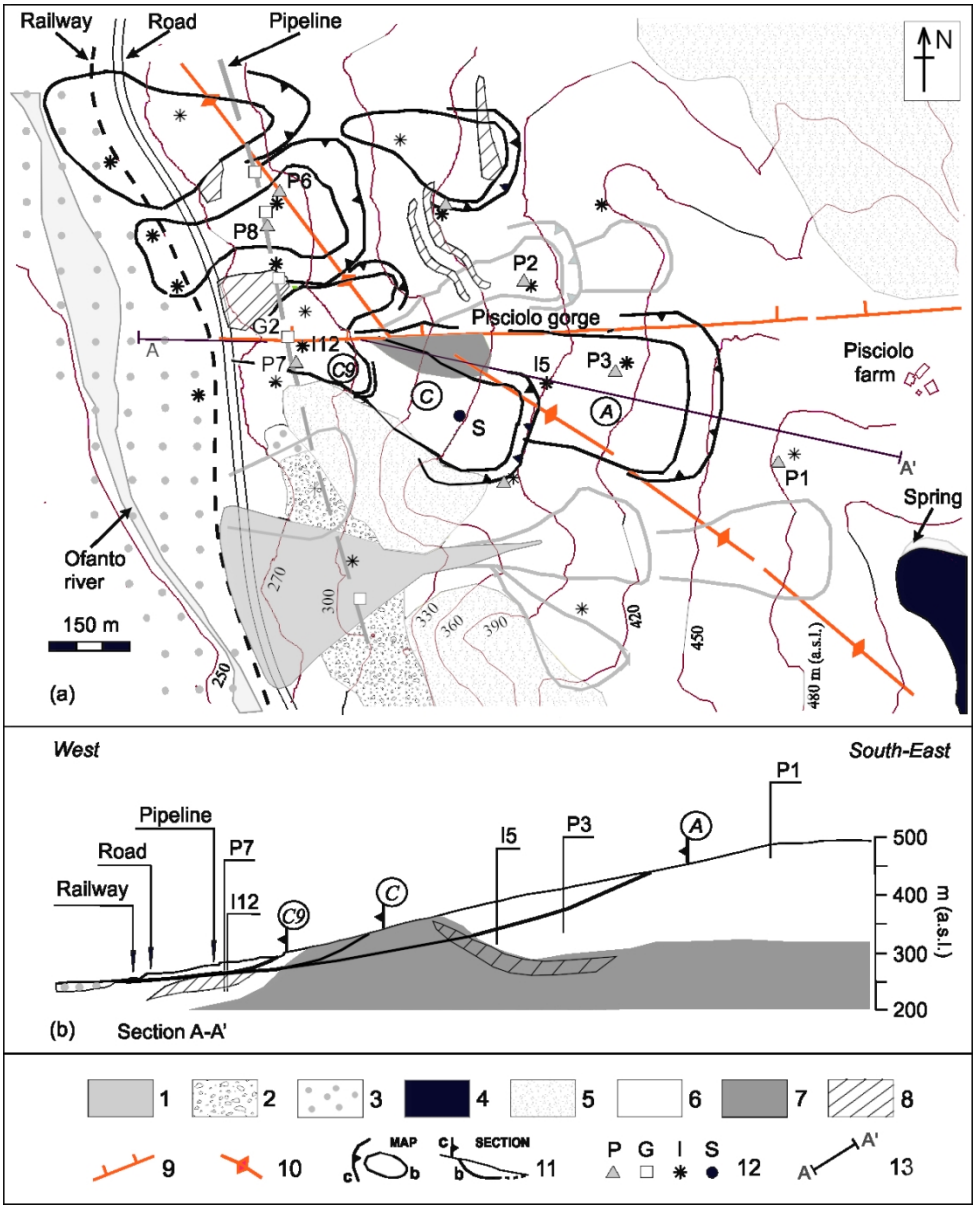


Figure 2. Geological map (a) and section (b) of the Pisciolo slope. Key: (1) fan deposit; (2) debris deposit; (3) alluvial deposit; (4) Pliocene succession; (5) Numidian Flysch Formation; (6) Paola Doce Formation; (7) Red Flysch Formation; (8) Fractured rock blocks and coarse inclusions; (9) fault; (10) anticline axis; (11) landslide body (b) and corresponding crown (c) (grey line when inactive); (12) P: boreholes equipped with piezometers; G: GPS antenna; I: boreholes equipped with inclinometers; S: area of shallow sampling; (13) section in plan (modified from Cotecchia et al. 2014).

© The Author(s) or their Institution(s)

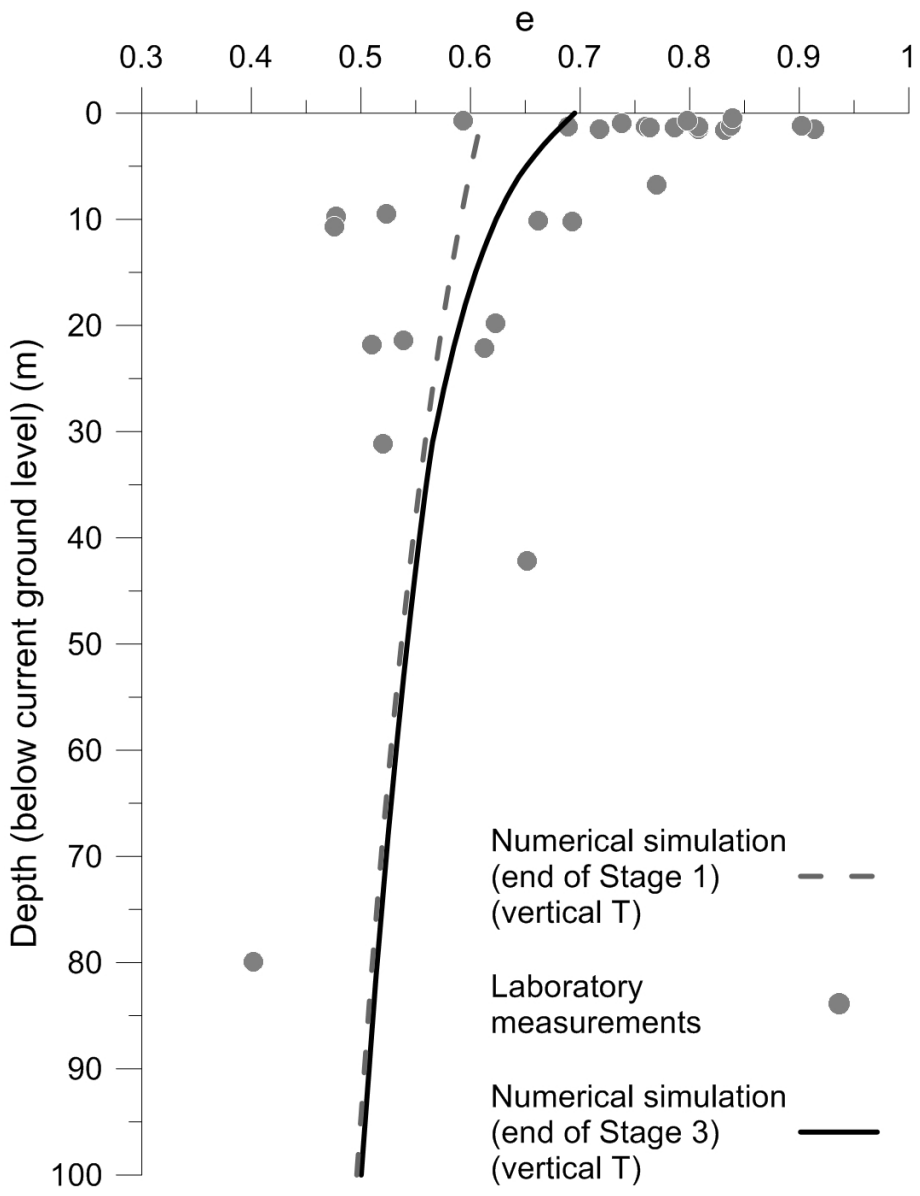


Figure 3. Void ratios measured on Paola Doce clay samples taken at Pisciolo at different depths compared with values predicted at key stages of the analysis (Table 3) along vertical T (Figure 9a).

© The Author(s) or their Institution(s)

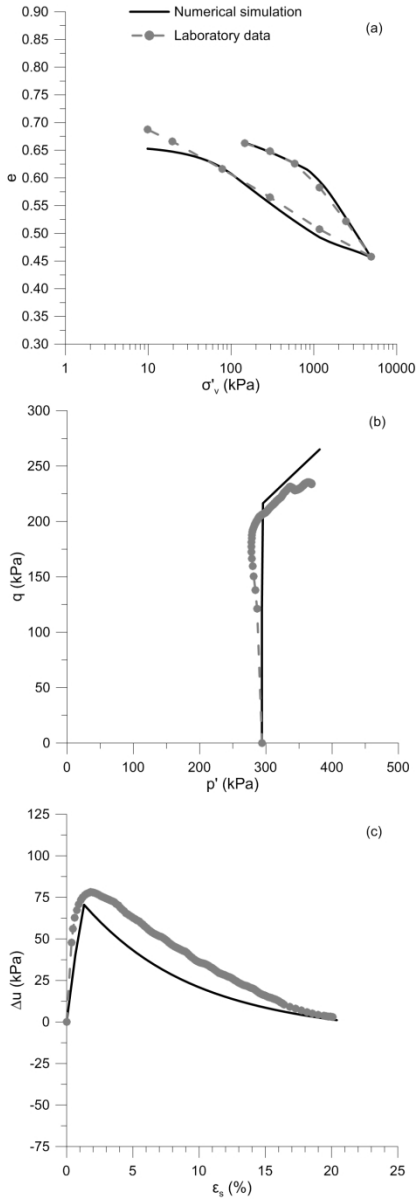


Figure 4. Comparison between experimental and numerical results for an oedometer test (a) and a triaxial test (b and c) conducted on Paola Doce clay samples taken at Pisciolo.

© The Author(s) or their Institution(s)

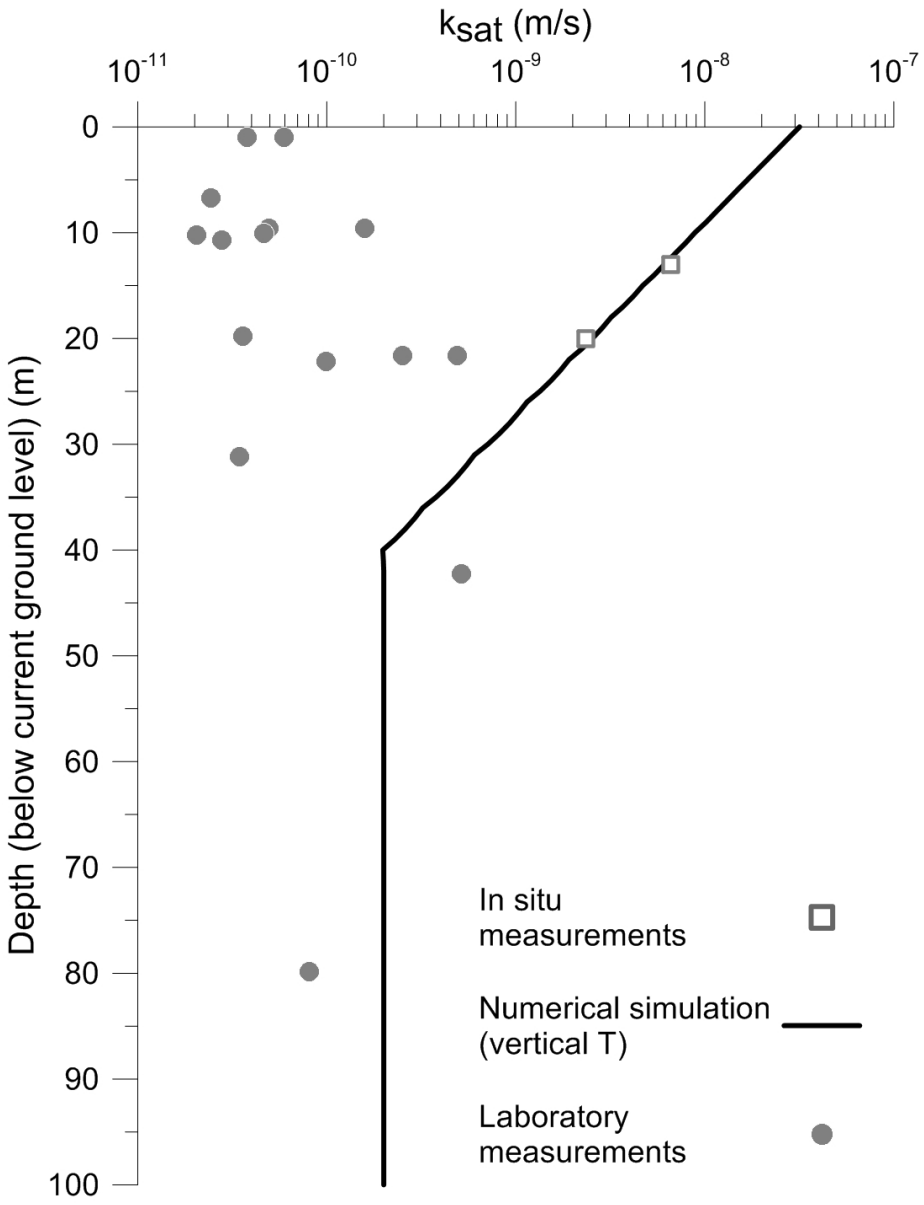


Figure 5. Saturated hydraulic conductivity profile assumed in the slope analysis compared with in situ measurements conducted at Pisciolo and saturated hydraulic conductivities estimated during oedometer tests carried out on Paola Doce clay samples taken at Pisciolo.

© The Author(s) or their Institution(s)

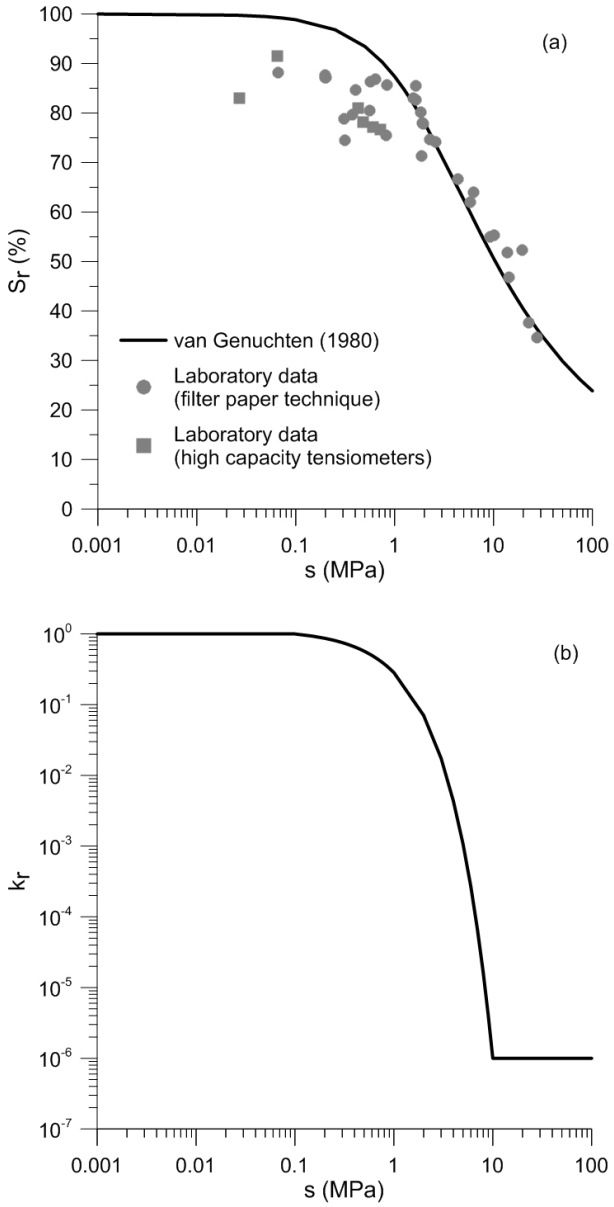


Figure 6. Water retention data measured on Paola Doce clay samples taken at Pisciolo at shallow depths (area S in Figure 2) compared with the water retention curve used in the analysis (a) and the corresponding hydraulic conductivity function adopted (b).

© The Author(s) or their Institution(s)

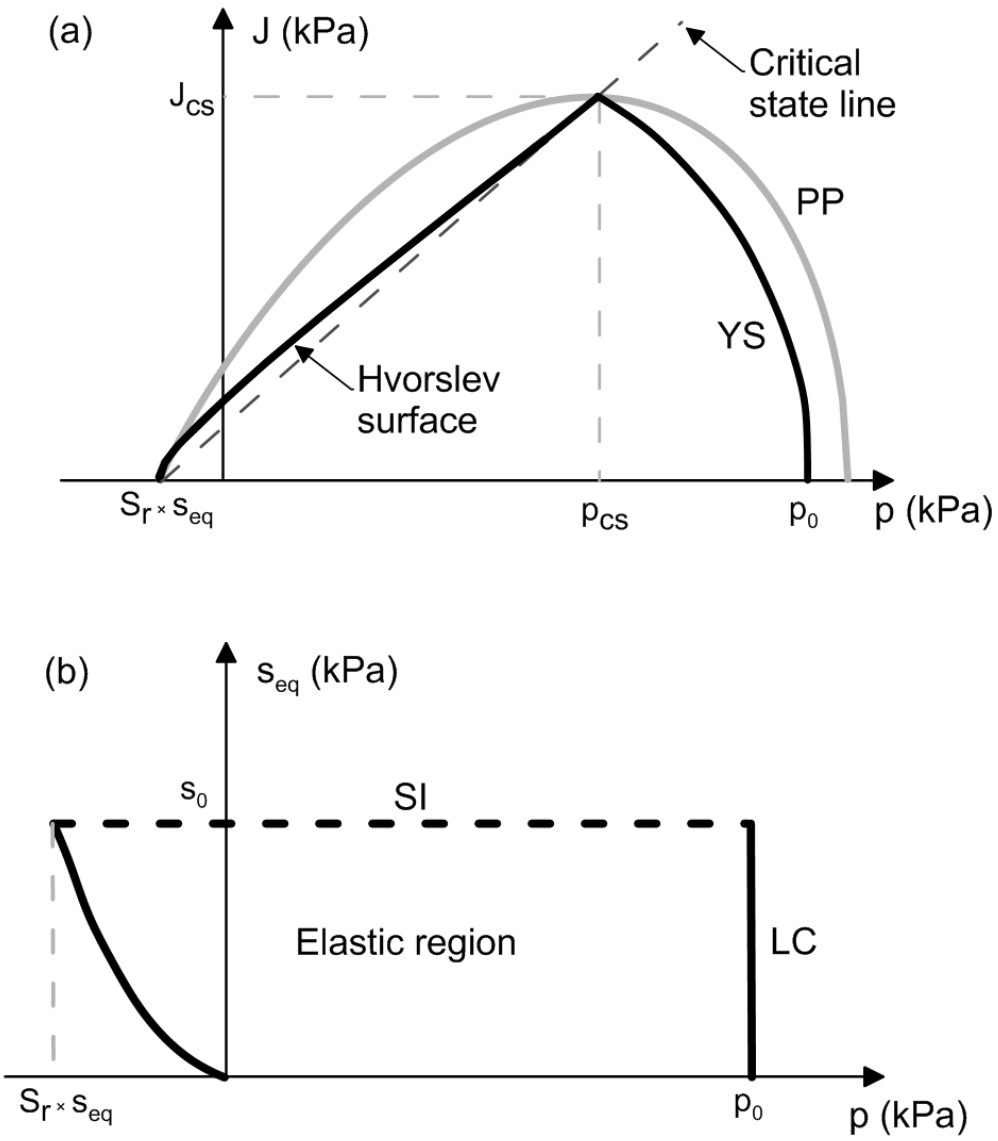


Figure 7. Yield surface (YS) and plastic potential (PP) of the constitutive model adopted in the analysis reported in the p-J (a) and p-s_{eq} (b) planes.

© The Author(s) or their Institution(s)

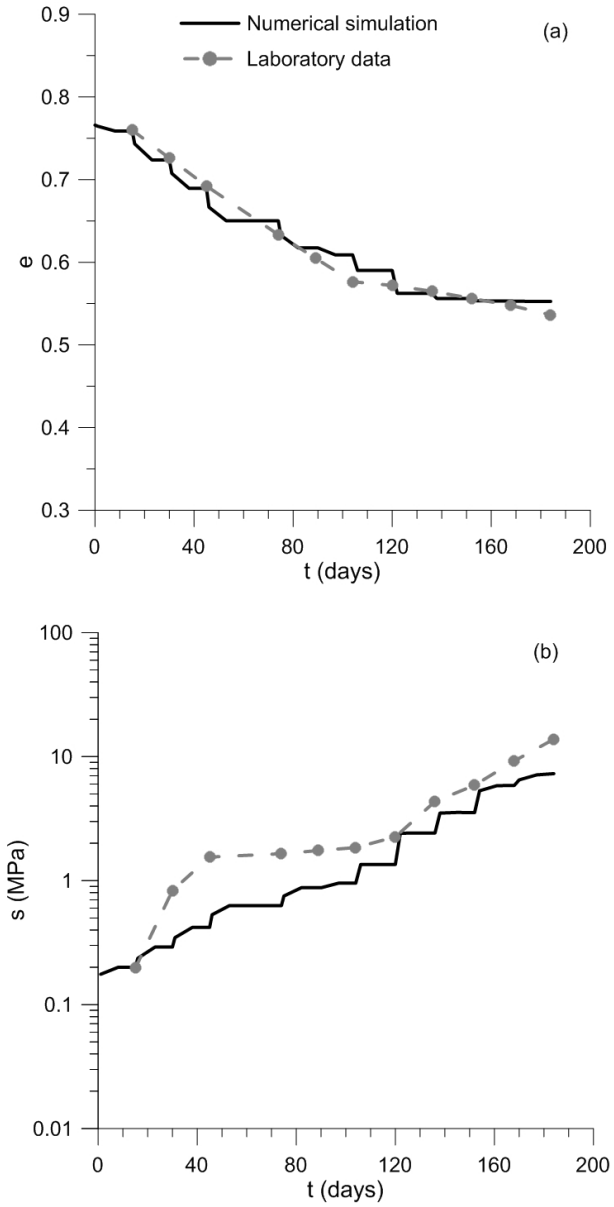


Figure 8. Variations of void ratio (a) and suction (b) with time for an unconfined drying test conducted on a Paola Doce clay sample taken at Pisciolo: comparison between experimental and numerical results.

© The Author(s) or their Institution(s)

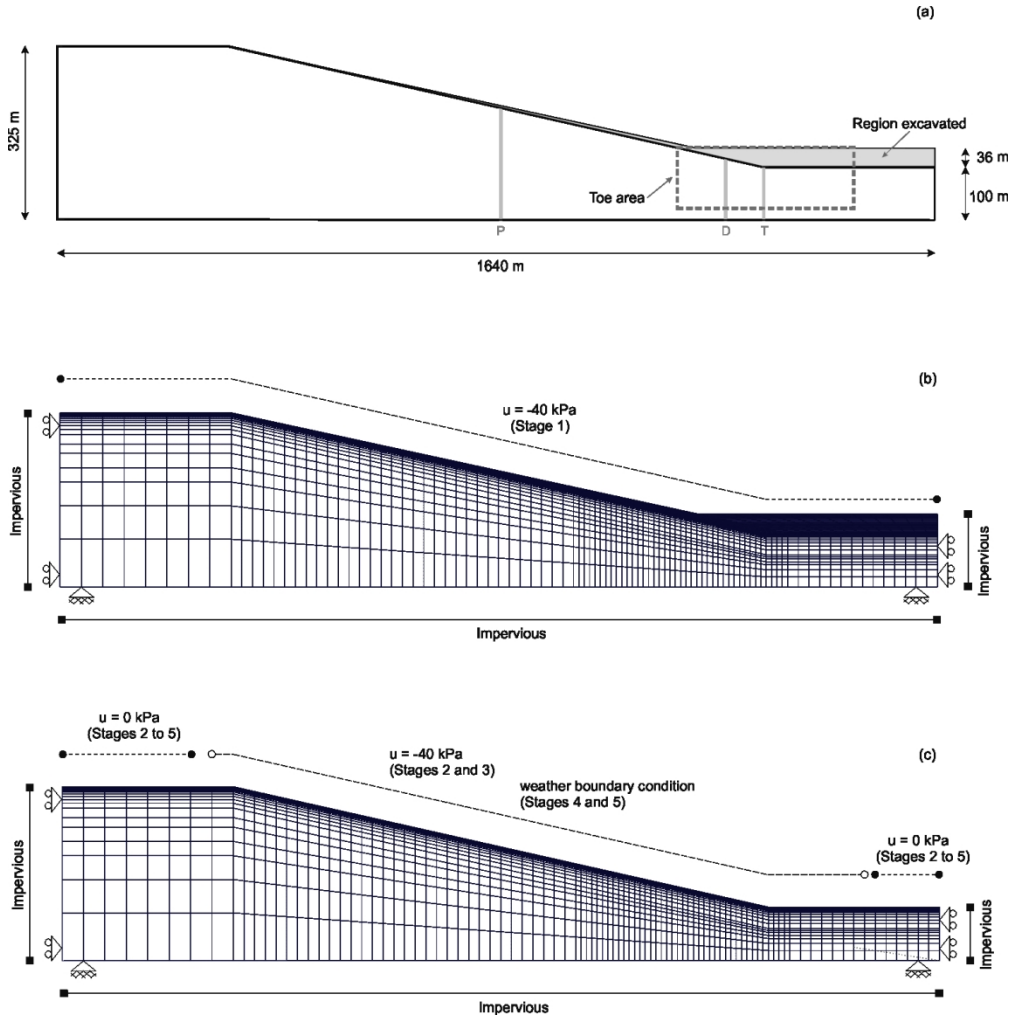


Figure 9. Geometry and dimensions of the slope analysed (a); mesh generated and boundary conditions adopted during Stage 1 (b) and Stages 2 to 5 (c).

© The Author(s) or their Institution(s)

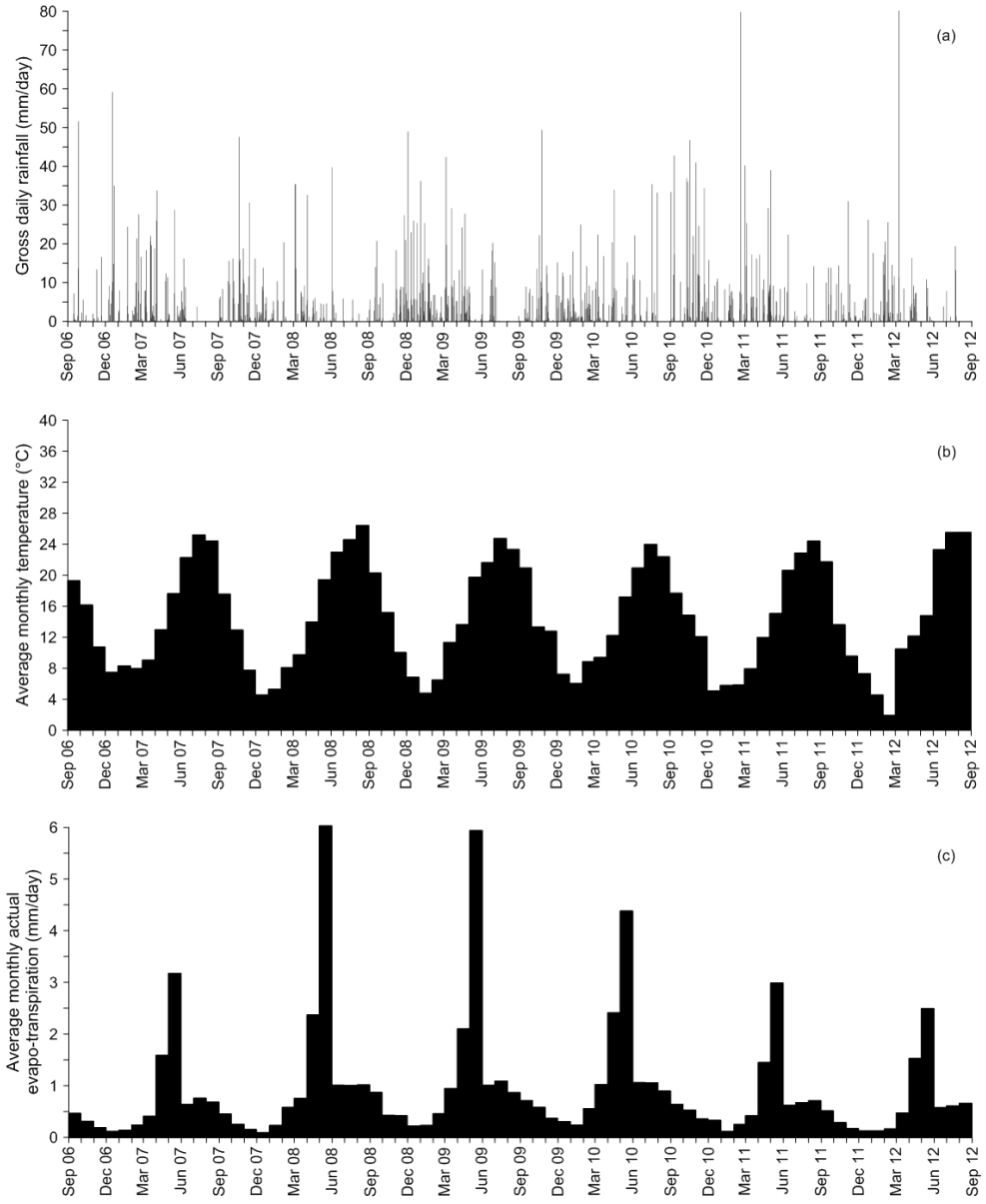


Figure 10. Gross daily rainfall (a) and average monthly temperature (b) measured at the Melfi weather station; average monthly actual evapo-transpiration estimated with the FAO Penman-Monteith method (Allen et al. 1998) (c).

© The Author(s) or their Institution(s)

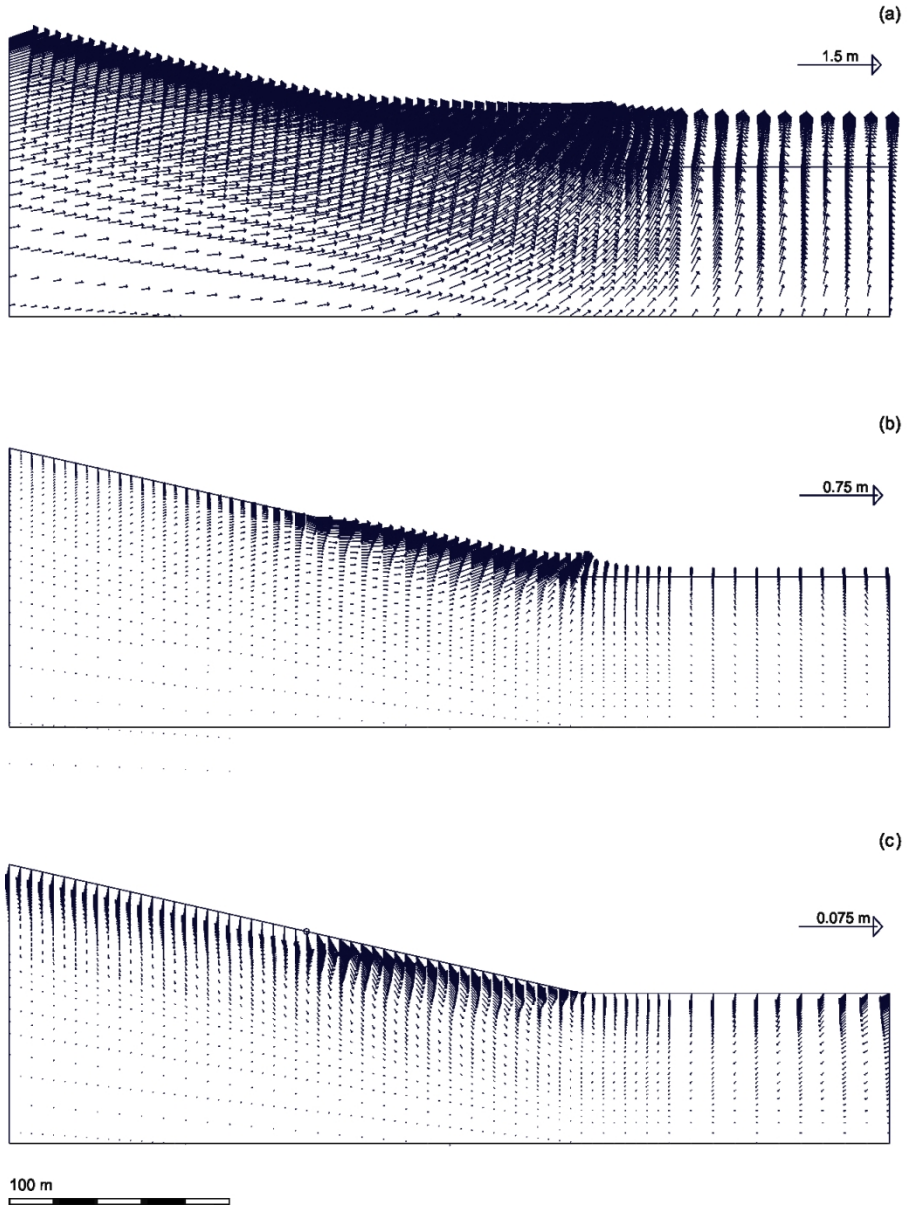


Figure 11. Displacements predicted: after modelling river erosion (a) (i.e. between end of Stage 1 and end of Stage 3); during Stage 4 only (b) (i.e. after simulating for 20 years the weather conditions recorded between 1 September 2006 and 31 August 2007); during Stage 5 only (c) (i.e. as a result of the weather conditions recorded between 1 September 2007 and 31 August 2012).

© The Author(s) or their Institution(s)

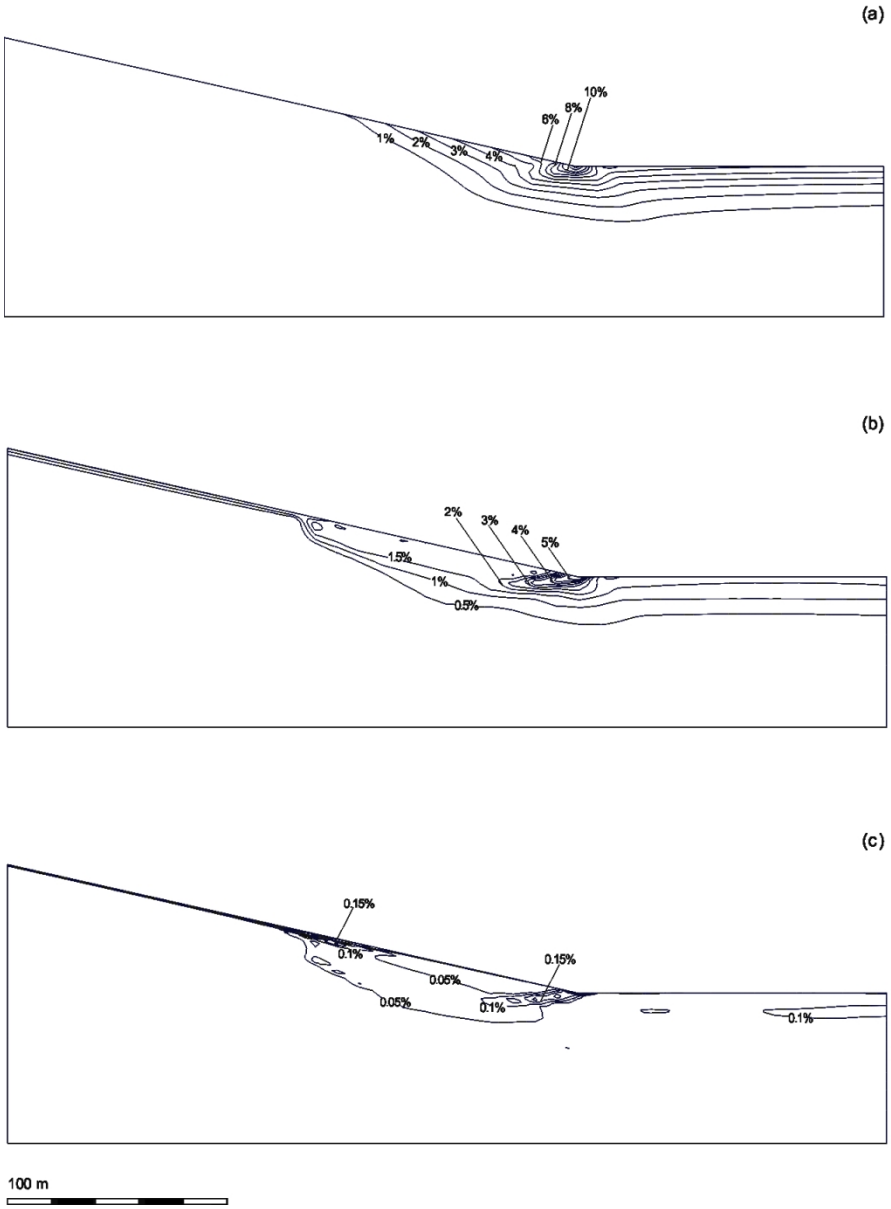


Figure 12. Contours of generalised deviatoric plastic strains predicted: after modelling river erosion (a) (i.e. between end of Stage 1 and end of Stage 3); during Stage 4 only (b) (i.e. after simulating for 20 years the weather conditions recorded between 1 September 2006 and 31 August 2007); during Stage 5 only (c) (i.e. as a result of the weather conditions recorded between 1 September 2007 and 31 August 2012).

© The Author(s) or their Institution(s)

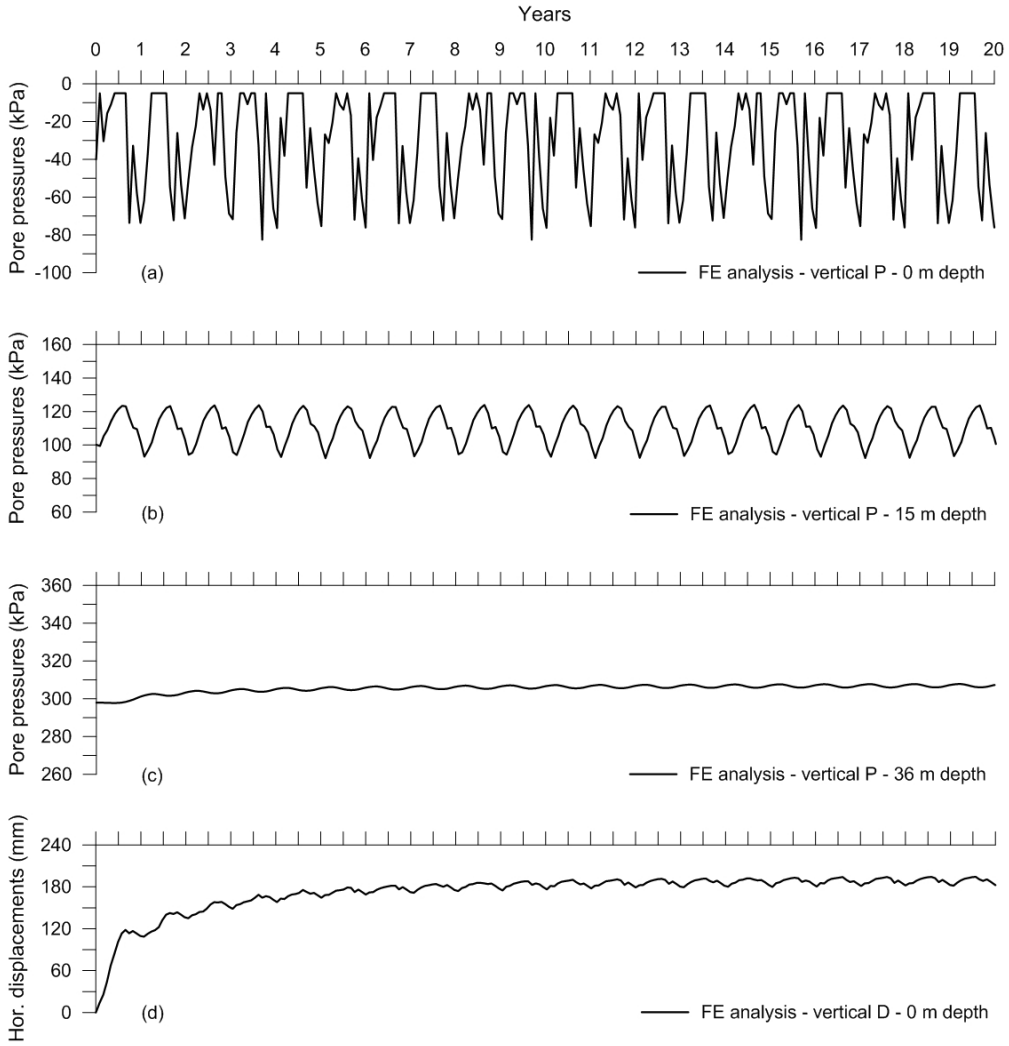


Figure 13. Pore water pressure variations predicted at 0 m (a), 15 m (b) and 36 m (c) depth along vertical P (Figure 9a) and horizontal displacement variations predicted at ground level (d) along vertical D (Figure 9a) as a result of a 'typical' year of weather (i.e. 1 September 2006-31 August 2007) assumed to act 20 consecutive times (Stage 4 in Table 3).

© The Author(s) or their Institution(s)

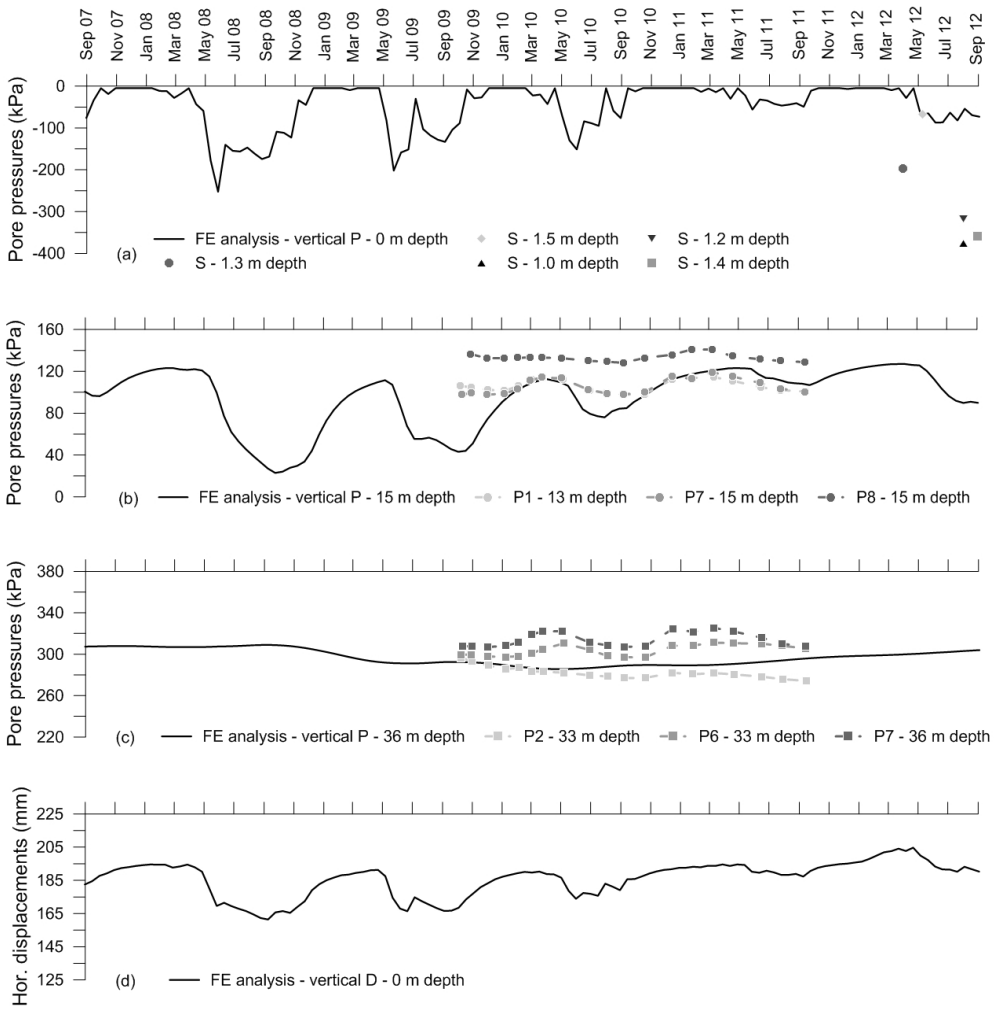


Figure 14. Pore water pressure variations predicted at 0 m (a), 15 m (b) and 36 m (c) depth along vertical P (Figure 9a) as a result of the weather conditions recorded between 1 September 2007 and 31 August 2012 compared with pore pressures measured at 1.0-1.5 m depth (a), 13-15 m depth (b) and 33-36 m depth (c); horizontal displacements predicted at ground level (d) along vertical D (Figure 9a) as a result of the weather conditions recorded between 1 September 2007 and 31 August 2012.

© The Author(s) or their Institution(s)

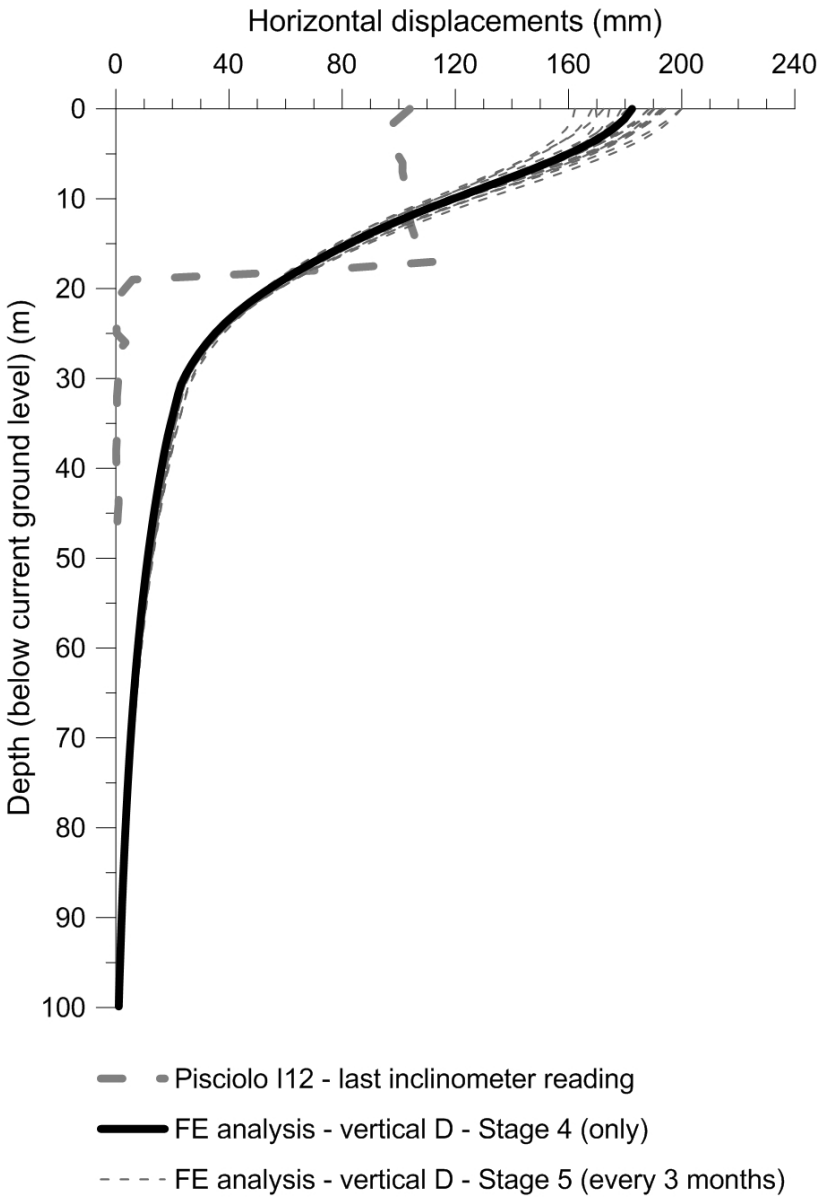


Figure 15. Profiles of horizontal displacements predicted along vertical D (Figure 9a) compared with the last inclinometer reading collected at Pisciolo through inclinometer I12 (Figure 2).

© The Author(s) or their Institution(s)